COMMUNICATION

Nanocomposites from Solution-Synthesized PbTe-BiSbTe Nanoheterostructure with Unity Figure of Merit at Low-Medium Temperatures (500–600 K)

Biao Xu, Matthias T. Agne, Tianli Feng, Thomas C. Chasapis, Xiulin Ruan, Yilong Zhou, Haimei Zheng, Je-Hyeong Bahk, Mercouri G. Kanatzidis, Gerald Jeffrey Snyder,* and Yue Wu**

More than 50% of the world's energy consumption is wasted in the form of heat, and thermoelectric energy conversion is attracting great attention as an effective and reliable method to recover this waste heat as electricity.[1] The efficiency of a thermoelectric material is determined by its dimensionless figure of merit, $zT = S^2\sigma T/(\kappa_e + \kappa_l + \kappa_{bi})$, where S is the Seebeck coefficient, σ is the electrical conductivity, T is the operating temperature, and κ_e, κ_l, and κ_{bi} are the electronic, lattice, and bipolar contributions to thermal conductivity, respectively. Maximizing zT requires the simultaneous enhancement of the power factor ($S^2\sigma$) and reduction of the thermal conductivity (κ_{tot}). Band engineering with resonant levels,[2] band convergence,[3] energy filtering effects,[4] and quantum confinement[5] are widely explored to enhance $S^2\sigma$. To reduce κ_{tot}, materials with an intrinsically low κ_l are used as the starting material.[6] Nanostructuring[7–9] and defect engineering[10] lead to further reduction in κ_l. As κ_{bi} is determined by electronic transport, it can be mitigated by degenerately doping the semiconductor and/or alloying it with larger-bandgap compounds.

Since the 1950, Bi_2Te_3-based alloys ($Bi_xSb_{2-x}Te_3$ and $Bi_2Te_{3-x}Se_x$) have been widely used and commercialized for refrigeration and thermoelectric energy conversion applications in the low-temperature range (300–450 K).[11–13] However, at higher temperatures (>500 K), their zT value decreases substantially, mainly due to the onset of bipolar conduction that arises from low carrier concentrations and its small bandgap ($E_g \approx 0.18$ eV). At mid-range temperatures (600–900 K), good candidates are mainly limited to PbTe alloys ($E_g \approx 0.31$ eV).[14] Thus, combining p-type BiSbTe and PbTe may yield good thermoelectric materials with a peak zT value located in the low-medium temperature range (500–600 K). Indeed, aliovalent Pb, with less valence electrons than Bi(Sb), can act as an extrinsic acceptor for p-type BiSbTe.[15] Similarly, doping with other elements (Ag,[16] In,[17] Cu,[18] Zn[19]) may allow further tuning of the carrier concentration, thus optimizing the power factor and shifting the peak zT toward higher temperatures, but at the cost of carrier mobility. Carrier concentration can also be modified through defect engineering (e.g., Sb/Te antisites), although limitedly.[12,20] On the other hand, nanostructuring can suppress lattice thermal conductivity (κ_l).[8] Nanosizing was also proposed to suppress κ_{bi} through selectively blocking minority carriers in BiSbTe, although limited to below 400 K.[8,21] Additionally, alloying/doping may tailor the bandgap and Fermi level, diminishing bipolar conduction. Alas, without synergistic optimization of these interdependent parameters, unity zT cannot be achieved in Bi_2Te_3-based materials from 500 to 600 K, where the application of thermoelectrics is promising for the recovery of low-grade waste heat. Furthermore, conventional solid-state synthesis[22] requires high-temperature, energy-consuming processes to alloy or dope, with poor control over grain size. In contrast, solution synthesis has provided a more sustainable and efficient route to both doping/alloying and nanostructuring,[23] inspiring us to improve the performance of Bi_2Te_3.

Herein, we report the thermoelectric properties of Pb-doped BiSbTe nanocomposites derived from a scalable, solution-synthesized precursor made in 10 g batches. The nominal compositions are $Bi_{0.7}Sb_{1.3}Te_3$ with 0–4.0 at% Pb dopants. The as-obtained nanocomposites show an optimized power factor ($S^2\sigma$) that peaks at a higher temperature than previous BiSbTe compounds, a strongly reduced κ_l as compared to bulk-grain counterpart, a remarkably suppressed κ_{bi}, and a high zT (≈1.0)

Dr. B. Xu, Prof. Y. Wu
Department of Chemical and Biological Engineering
Iowa State University
Ames, IA 50011, USA
E-mail: yuewu@iastate.edu
M. T. Agne, Dr. T. C. Chasapis, Prof. G. J. Snyder
Department of Materials Science and Engineering
Northwestern University
Evanston, IL 60208, USA
E-mail: jeff.snyder@northwestern.edu
T. Feng, Prof. X. Ruan
School of Mechanical Engineering
Purdue University
West Lafayette, IN 47907, USA
Dr. Y. Zhou, Prof. H. Zheng
Materials Sciences Division
Lawrence Berkeley National Laboratory
Building 62 Room 211, 1 Cyclotron Road, Berkeley, CA 94720, USA
Prof. J.-H. Bahk
Department of Mechanical and Materials Engineering
University of Cincinnati
Cincinnati, OH 45221, USA
E-mail: bahkjg@uc.edu
Prof. M. G. Kanatzidis
Department of Chemistry
Northwestern University
Evanston, IL 60208, USA

DOI: 10.1002/adma.201605140

in the range of 513–613 K. This pushes the working temperature of conventional BiSbTe materials ≈100 K higher.

The low-temperature solution-phase synthesis is based on a three-step strategy developed by our group.[24,25] In Step 1, tellurium dioxide, potassium hydroxide, and polyvinylpyrrolidone (M_w = 40 000) are dissolved into ethylene glycol (EG). The pale yellow solution is then heated to 100 °C and hydrazine hydrate (80%) is injected. The solution turns into a dark blue slurry, indicative of the formation of tellurium (0). It is kept at 100 °C for 1 h before the temperature is raised to 110 °C. In Step 2, a solution of lead acetate trihydrate is added drop wise into the dispersion of Te nanowires at 110 °C. Then another 1 h of heating is maintained for the formation of the PbTe-Te-PbTe nanoheterostructure. In Step 3, an EG solution of Bi and Sb precursors (bismuth nitrate pentahydrate and antimony acetate) is added drop by drop, with precedent injection of anhydrous hydrazine. The black slurry is heated at 110 °C for 1 h and then incubated at 140 °C for another 8 h before the production of the PbTe-BiSbTe-PbTe nanoheterostructure.

Comprehensive characterization is performed to examine the structure and composition of the intermediate product at each step of the synthesis. First, X-ray diffraction (XRD) patterns are recorded to verify the crystal phases. After Step 1, pure Te (trigonal, JCPDS-#36-1452) is indexed and no impurity such as TeO_2 is found (**Figure 1**a). This corroborates the reducing ability of hydrazine hydrate, as evidenced by its wide use in efficient synthesis of Te nanostructures.[25] After Step 2, the diffraction peaks of both Te and PbTe (face centered cubic, JCPDS-#38-1435) are discerned, indicating that PbTe has been incorporated (Figure 1a). After Step 3, the XRD profile shows peaks of PbTe, Te, and $Bi_xSb_{2-x}Te_3$ (hexagonal, x = 0.5 for JCPDS-#49-1713) (Figure 1a). However, as some reflection peaks of Te, PbTe, and $Bi_xSb_{2-x}Te_3$ overlap with each other, transmission electron microscopy (TEM) investigation is needed for further clarification.

The compositions of the aforementioned nanostructures are further verified by our TEM study. First, the 1D shape of the Te nanowire, produced in Step 1, is clearly observed (Figure 1b). Statistics of the nanowire diameter reveal a narrow distribution (17 ± 2 nm) and the length of nanowires is found to be 1500 ± 200 nm. The (001) lattice fringe of Te (**Figure 2**a) that is perpendicular to the axial direction indicates that the nanowire grows along the c axis. Second, in Figure 1c, the barbell-like morphology of the PbTe-Te-PbTe nanoheterostructure is displayed. The (111) plane of PbTe can be seen on the tips and is parallel with the (001) plane of Te wire part (Figure 2b). After step 3, all the crystal domains of Te, PbTe, and $Bi_xSb_{2-x}Te_3$ can be found in the as-obtained PbTe-BiSbTe-PbTe nanoheterostructure (Figure 1d and 2c,d). The PbTe (002) lattice fringe is found on the tip. A fast Fourier transform (FFT) pattern along the Te [010] zone axis is observed on the nanowire body. The typical layered structure and (006) spot of $Bi_xSb_{2-x}Te_3$ in FFT are seen on the sidewall of the nanowire (Figure 2c) and also the junction of the wire and the tip (Figure 2d). This indicates that $Bi_xSb_{2-x}Te_3$ is grown from the reaction of Bi and Sb atoms with surface Te atoms. High angular annular dark field-scanning transmission electron microscopy (HAADF-STEM) and elemental mapping also corroborate that PbTe is grown on the tip, while the nanowire body is comprised of $Bi_xSb_{2-x}Te_3$ and unreacted Te (Figure 2e).

Scanning electron microscopy (SEM) images further verify the morphology of products step-by-step (Figure S1–S4,

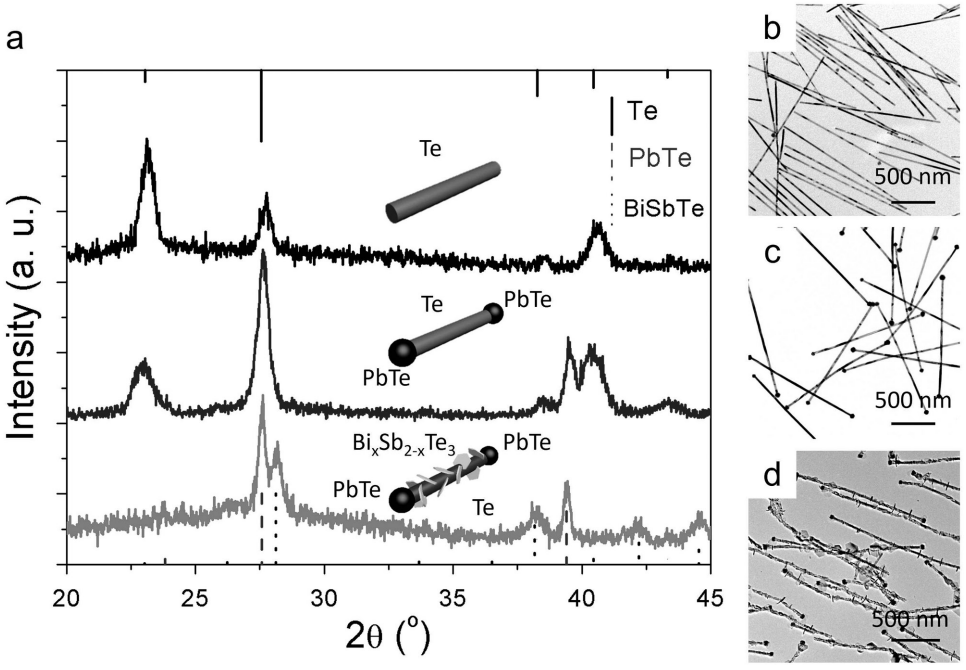

Figure 1. Characterization of the intermediate products of the PbTe-BiSbTe nanoheterostructure. a) XRD patterns of Te (top) after step 1, 0.04 PbTe-Te-PbTe (middle) after step 2, and 0.04 PbTe-BiSbTe-PbTe (bottom) after step 3; the solid lines are indicative of tellurium, the dashed ones are PbTe, and dotted ones represent $Bi_{0.5}Sb_{1.5}Te_3$. Transmission electron microscopy images of b) Te nanowire, c) 0.04 PbTe-Te, and d) 0.04 PbTe-BiSbTe nanoheterostructure.

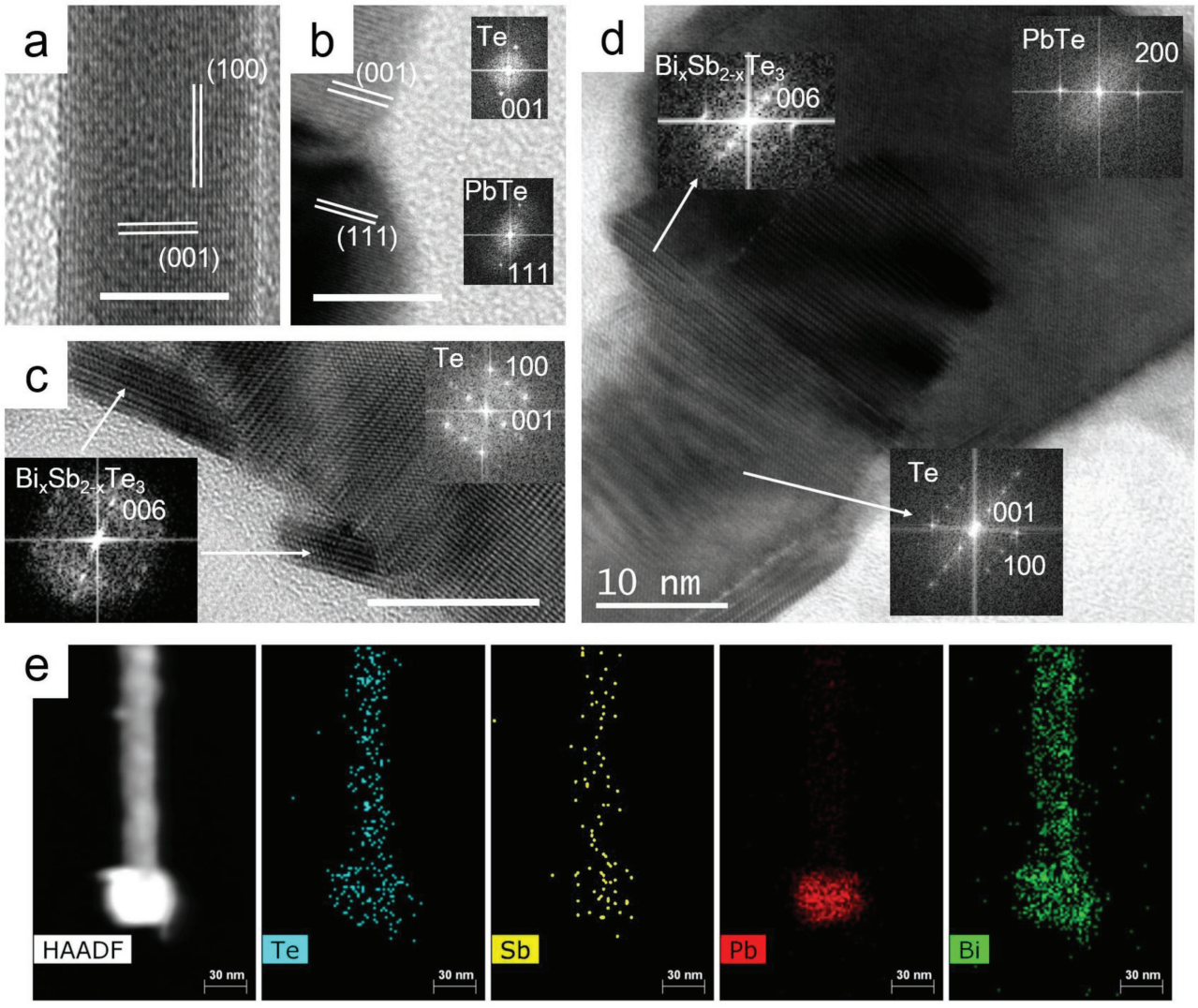

Figure 2. HRTEM study on intermediate products of the PbTe-BiSbTe nanoheterostructure. HRTEM images of a) the Te nanowire after step 1, b) the 0.04 PbTe-Te-PbTe nanoheterostructure after step 2, c) the wire part and d) the junction area of the 0.04 PbTe-BiSbTe-PbTe nanoheterostructure after step 3. The insets show corresponding fast Fourier transform (FFT) patterns. All scale bars in (a)–(d) represent 10 nm. e) HADDF-STEM image and EDS elemental mapping of the 0.04 PbTe-BiSbTe-PbTe nanoheterostructure; the scale bar is 30 nm.

Supporting Information). Energy-dispersive spectrum (EDS) also provides strong evidence that the Te nanowire is only partially converted to BiSbTe in the PbTe-BiSbTe-PbTe nanoheterostructure. Taking the "0.015 Pb" sample as an example, the atomic ratio of Pb:Bi:Sb:Te is 1.5:16.3:49.0:100 in the precursors. While the atomic ratio in the final product is Pb:Bi:Sb:Te = 1.4:16.9:27.9:100. It is clear that Pb, Bi, and Te are mostly converted, whereas only ≈57% (27.9/49.0) of Sb is reacted.

The successful synthesis of the PbTe-BiSbTe nanoheterostructure and its structural integrity may originate from the delicate match in atomic structure of each constituent phase. According to high resolution transmission electron microscopy (HRTEM) analyses (Figure 2), we construct atomic structure models for PbTe (111)-Te (001), $Bi_xSb_{2-x}Te_3$ (001)-Te (001), and PbTe (111)-$Bi_xSb_{2-x}Te_3$ (001) interfaces (Figure S5–S10, Supporting Information). In these models, the dangling bonds are well saturated and the coordination geometry is finely retained at the interfaces. The nice match in crystal structures also brings about the generality in synthesis. The composition of these PbTe-BiSbTe-PbTe nanoheterostructures is tunable over a wide range (0.5–4.0 at% Pb, see the Experimental Section in the Supporting Information; Figure S3 and S4 of the Supporting Information and Figure 2). This provides us with a rich library of potentially new materials. The other important feature of our synthesis is the 10 g scale (**Figure 3**a, inset). To the best of our knowledge, this is the first synthesis of nanoheterostructures in such an energy-saving, repeatable and scalable way. The scalable synthesis of nanoheterostructures will pave the way for applications not only in thermoelectrics but also in other fields, such as photocatalysis, electronics, and optoelectronics.[26]

The tunable, repeatable, and scalable synthesis of PbTe-BiSbTe nanoheterostructures allows us to fabricate bulk nanocomposites. The nanoheterostructures are washed by an ethanol solution of hydrazine and then vacuum dried.[24] The

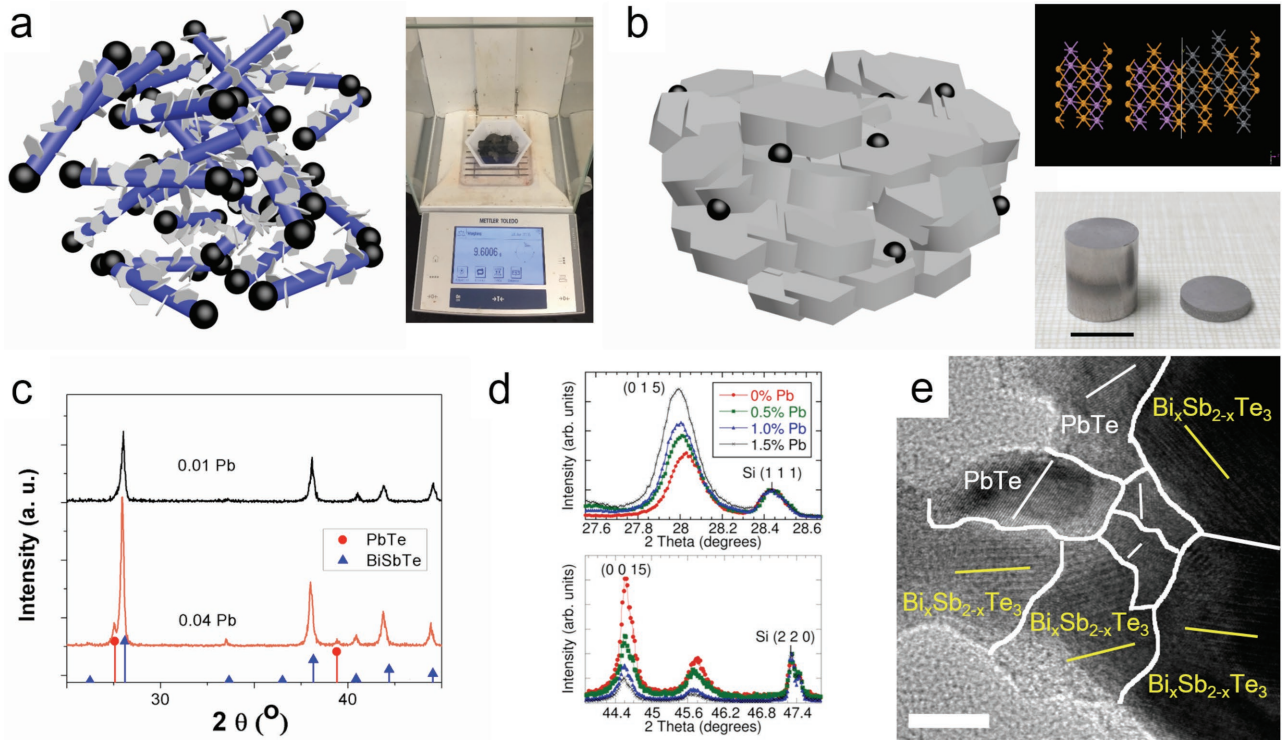

Figure 3. Characterization of the Pb-BiSbTe nanocomposites after SPS. a) Schematic illustration and digital image of 9.6 g of nanoheterostructures before SPS; b) Schematic illustration of as-pressed Pb-BiSbTe nanocomposite, atomic structure of PbTe-BiSbTe interface (purple: Bi/Sb; gray: Pb; and orange: Te) and digital image of the SPSed cylinder and disk; scale bar is 10 mm. c) XRD profiles of the 0.01 PbTe and 0.04 PbTe-$Bi_{0.7}Sb_{1.3}Te_3$ bulk nanocomposites. The red drop line indicates PbTe and the blue one corresponds to $Bi_{0.5}Sb_{1.5}Te_3$; d) XRD peak shifts corresponding to increased lattice parameters with nominal Pb doping; e) HRTEM image of 0.04 PbTe-$Bi_{0.7}Sb_{1.3}Te_3$ bulk nanocomposite. The white lines depict lattice fringes of PbTe and the yellow ones stand for those of BiSbTe. The scale bar is 10 nm.

dried chunk is ground into a fine powder and filled into a phi-10.0 mm (inner diameter) graphite die in a glove box. Then the tooling is loaded in a Fuji-211lx Spark Plasma Sintering (SPS) system where it is put under vacuum and subjected to a uniaxial pressure of 40 MPa, heated and kept at 425 °C for 5 min. The as-obtained disk is polished and shows metallic luster (Figure 3b, inset).

The compositions of the SPSed disks are checked via EDS. For the 0.015 Pb sample, the Pb:Bi:Sb:Te molar ratio is around 1.4:16.1:30.2:71.1. Compared with the nanoheterostructure before SPS (Pb:Bi:Sb:Te molar ratio = 1.4:16.9:27.9:100), it is clear that the ratio among Pb, Bi, and Sb is almost unchanged. In contrast, there is a 28.9% loss of Te. Before SPS, the molar ratio of Te/(Bi+Sb) is 2.23 in the pristine powder, which is significantly larger than 1.50, a typical value for $Bi_{0.7}Sb_{1.3}Te_3$. The pristine powder can be regarded as Pb-$Bi_{0.7}Sb_{1.3}Te_3$ alloy plus excess elemental Te. According to the Te-rich region of the $Bi_xSb_{2-x}Te_3$-Te phase diagram,[10] the Te nanowire melts above ≈420 °C. Therefore, during the SPS process (≈425 °C), liquid Te is expelled out of the nanocomposite, leaving $Bi_{0.7}Sb_{1.3}Te_3$ nanoflakes and PbTe nanograins compressed together (Figure 3b), with an effective grain size of 40–60 nm (Figure 3e). In the final nanocomposite, the molar ratio of Te/(Bi+Sb) is 1.53, which is quite approximate to the stoichiometric value of 1.50. Similar trends are also found in the 0.01 Pb sample. Before SPS, the Pb:Bi:Sb:Te molar ratio is around 0.8:17.1:25.7:100. After SPS it is 0.8:16.1:28.1:70.0. The Pb:Bi:Sb:Te molar ratio in the after-SPS 0.005 Pb sample is 0.4:14.0:25.2:60.2. For the undoped (0% Pb), after-SPS, sample the Bi:Sb:Te molar ratio = 14.3:25.6:60.2.

In the final PbTe-$Bi_{0.7}Sb_{1.3}Te_3$ nanocomposites, Pb may be dissolved in $Bi_{0.7}Sb_{1.3}Te_3$ or precipitate out as PbTe inclusion.[27] In SEM-EDS elemental mapping of 0.01 PbTe-$Bi_{0.7}Sb_{1.3}Te_3$, Pb is found to be scattered throughout the sample (Figure S13, Supporting Information). The dissolution of Pb in $Bi_{0.7}Sb_{1.3}Te_3$ is revealed by the progressive shift in the XRD peak of $Bi_{0.7}Sb_{1.3}Te_3$ (0 1 5) and (0 0 15) toward lower 2θ (higher interplane distance; Figure 3d), as the atomic radius of Pb is larger than Bi(Sb). The dissolved Pb is expected to act as an acceptor to parent $Bi_{0.7}Sb_{1.3}Te_3$ because there is one less valence electron in Pb ($6s^26p^2$) than in Bi ($6s^26p^3$, Sb, $5s^25p^3$). This leads to p-type conduction in the as-obtained disk, as is proved by the Hall effect measurement (Figure S14a, Supporting Information). The efficient doping of Pb may be aided by the small grain size of the starting PbTe-BiSbTe nanoheterostructures, which readily facilitates diffusion of Pb into BiSbTe during SPS. For the 0.01 Pb sample, the reflection peaks of PbTe are not detectable in XRD (Figure 3c). As the concentration of Pb increases (e.g., for 0.04 Pb sample) and exceeds the solubility limit in BiSbTe, PbTe can precipitate out as inclusions, as proved by XRD (Figure 3c, lower pattern) and TEM (Figure 3e).

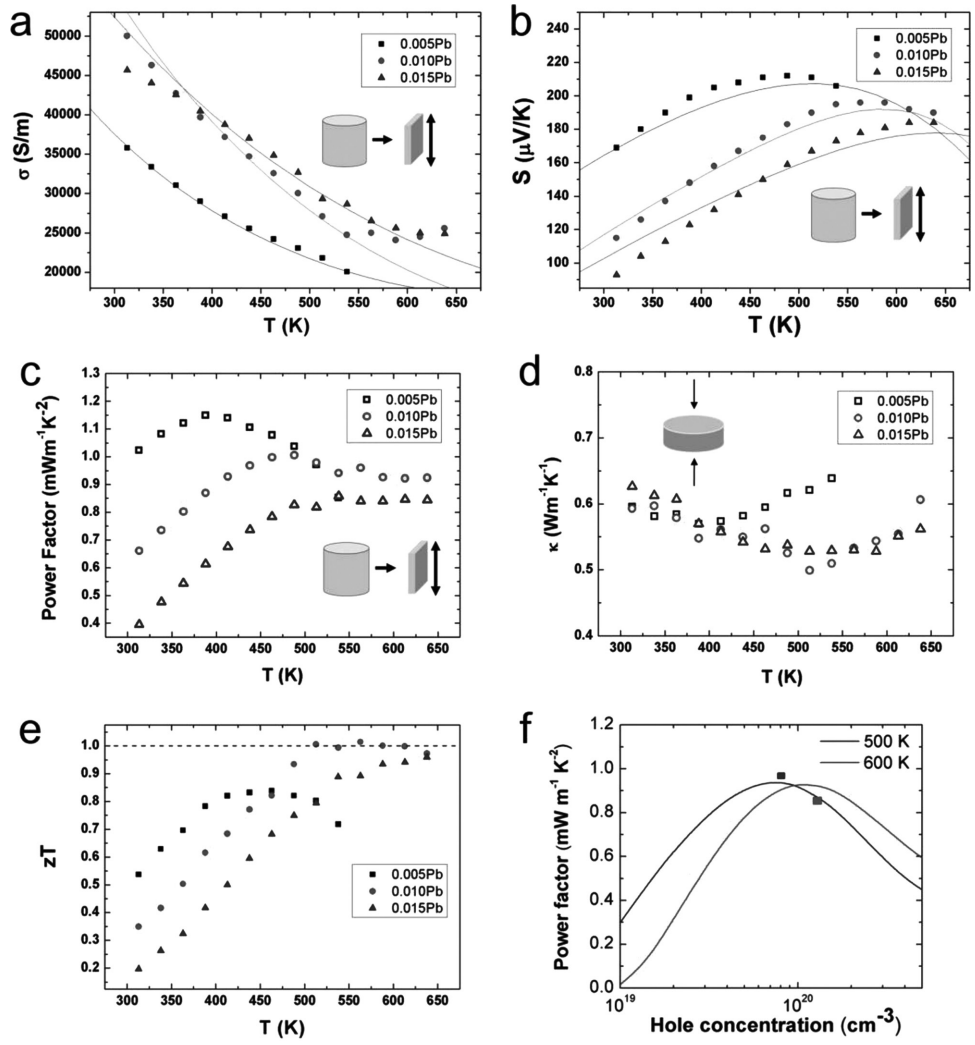

Figure 4. Measurements and simulations of thermoelectric properties. Temperature dependence of a) electrical conductivity, b) Seebeck coefficient, c) power factor, d) thermal conductivity, and e) figure of merit. f) BTE-calculated power factor ($S^2\sigma$) as a function of hole concentration (curves) with experimental values (markers). The markers in (a)–(f) are experimental values and the curves in (a), (b), and (f) are simulations.

The successful fabrication of PbTe-BiSbTe bulk nanocomposites with tunable composition enables us to investigate their thermoelectric properties. Unless intentionally noted, all measurements are conducted in the cross-plane direction (**Figure 4**; also see in-plane results in Figure S15, Supporting Information). Electrical conductivities (σ) of the 0.005, 0.010, and 0.015 Pb samples all decrease with ascending temperature, as is typical of heavily doped degenerate semiconductors (Figure 4a). While in the high-temperature intrinsic region, σ of the 0.010 Pb sample shows saturation. The 0.015 Pb sample has similar electrical conductivity with that of the 0.010 Pb sample and higher σ than that of the 0.005 Pb sample. Hole concentration (n_p) increases monotonically with increased Pb composition (8.00×10^{19} cm^{-3} for 0.010 Pb sample and 1.25×10^{20} cm^{-3} for 0.015 Pb sample; Figure S14a, Supporting Information) while the hole mobility (μ_p) shows the opposite trend (Figure S14b, Supporting Information).

Composition-dependent Seebeck coefficients (S) are presented in Figure 4b. For the 0.005, 0.010, and 0.015 Pb samples, the S have positive signs, agreeing well with the Hall-effect measurements showing a p-type transport behavior (Figure S14a, Supporting Information). The Seebeck coefficients increase steadily with rising temperature in the low-temperature range and then decrease afterward with elevated temperature. This roll-over behavior can be attributed to the thermal excitation of minority carriers (electrons) and their adverse contribution to the net Seebeck coefficient. The decreased Seebeck coefficients with respect to increased carrier concentration can be explained by the Pisarenko plot (S-n_H) (Figure S14g, Supporting Information). Power factors ($S^2\sigma$; Figure 4c) for all the samples first exhibit increment with rising temperature in the low-temperature range before reaching plateau. The maximum power factors of the 0.005, 0.01, and 0.015 Pb samples are 1.15, 1.00, and 0.86 mW m^{-1} K^{-2}, respectively.

The thermal conductivity can be expressed by $\kappa = C_p \times D_T \times \rho$, where C_p (J g^{-1} K^{-1}) is the specific heat obtained by differential scanning calorimetry (Figure S14c, Supporting Information), D_T (m^2 s^{-1}) is the thermal diffusivity measured by the laser flash method (Figure S14d, Supporting Information), and ρ is the density (≈5.30 g cm^{-3}, relative density = 78%, determined geometrically). The dependence of total thermal conductivity (κ_{tot}) on temperature is presented in Figure 4d. The κ_{tot} of the 0.005 Pb sample decreases from 0.60 W m^{-1} K^{-1} at 313 K to 0.57 W m^{-1} K^{-1} at 388 K and then increases to 0.64 W m^{-1} K^{-1} at 538 K. Similarly, the κ_{tot} of the 0.010 Pb and 0.015 Pb samples show an initial decrease and subsequent increase as the temperature goes high.

Finally, the temperature dependence of figure of merit is plotted in Figure 4e. Clearly the zT of the 0.005 Pb sample is better than those of the other two compositions below 450 K, reaching a peak of 0.84 at 438 K, but starts to drop at >450 K. The zT of the 0.010 Pb sample increases from 0.35 (at 313 K) to 1.02 (at 513 K) and maintains higher than 1.0 (at 613 K) before dropping below 1.0 (0.95 at 638 K). The zT of the 0.015 Pb sample increases steadily from 0.21 (at 313 K) to 0.95 (638 K). Moreover, the high performance is maintained the same after repeated tests (Figure S16, Supporting Information). The thermoelectric properties of the 0.020 and 0.040 Pb samples are also shown in Figure S15f,g (Supporting Information).

To investigate the origin of the high zT values in the low-medium temperature (513–613 K) range, we have conducted a series of experimental analysis and theoretical modeling. First, diffuse reflectance Fourier transform infrared spectroscopy is used to determine the optical bandgap for several Pb concentrations at room temperature (**Figure 5**d and Figure S17, Supporting Information). By definition of the Burstein–Moss effect, $E_g = E_{g,0} + \Delta E_g^{BM}$ (dashed line in Figure 5d), increased degeneracy pushes the Fermi level deeper into the band (valance band for our p-type material), causing the effective bandgap, E_g, to widen as minority carriers must not only cross the intrinsic bandgap, E_{g0}, but also reach the lowest unoccupied level in the band. The extra energy required for these carriers to cross the gap is called the Burstein–Moss shift, defined in the context of parabolic bands as $\Delta E_g^{BM} = (\hbar^2/2\, m_{vc}^*)(3\pi^2 n)^{2/3}$ where m_{vc}^* is the reduced effective mass of the valance and conduction band (a value of unity was used in Figure 5d), and n is carrier concentration. While there may be a renormalization term added to account for carrier screening effects,[28] the trend in the observed optical gap with Pb concentration (Figure 5d) clearly follows a Burstein–Moss-type behavior, as also seen in Pb-doped Bi_2Te_3 (values shown as green squares in Figure 5d were calculated from data taken from ref. [29]). The increase in effective bandgap is further corroborated by the observed increase in the Goldsmid–Sharp gap[30] (Table S1 and blue markers in Figure S17b, Supporting Information) calculated empirically from the Seebeck data.

Generally, theoretical modeling of the electrical conductivity and Seebeck coefficient of different Pb-BiSbTe samples is done using the Boltzmann transport equation (BTE).[31] We considered both conduction and valence bands in the modeling to quantify the bipolar transport effect on these material properties. The band structure parameters used in the BTE simulation were obtained by fitting the electronic density of states (DOS) of Bi_2Te_3 from the first-principle band structure calculations.[32] We used the modified Kane model in the DOS fitting to account for the nonparabolicity in the bands, and included two conduction bands and two valence bands to fit the DOS over a wide energy range.[31] More information can be found in the Supporting Information. The same band parameters that were used for Bi_2Te_3 were used for our materials except for the bandgap, which was adjusted to best fit the experimental electrical conductivities and Seebeck coefficients of our samples. As a result, a bandgap of 0.22 eV was used in our simulations, and this value is consistent with the Goldsmid–Sharp energy gap (Table S1, Supporting Information). Note that this bandgap value used in our BTE simulation does not include the Burstein–Moss shift shown in the optical bandgap. **Table 1** summarizes the band structure and material parameters used in the BTE simulation. As shown in Table 1, the hole mobility is reduced with increased Pb, which is due to the increased carrier scattering with defects and interfaces.

The calculated electron transport properties are shown as solid curves in Figure 4a,b, and match well with the experimental results (markers in Figure 4a,b). With increased Pb doping and corresponding higher carrier concentration, the Pb-BiSbTe samples show an increased Fermi level away from the valence band maximum, according to BTE calculations (Figure S14e, Supporting Information), in agreement with the Burstein–Moss shift discussed above. Increased majority carrier (hole) concentration, occupying higher energy levels, results in reduced thermal excitation of minority carriers (electrons), thus the net Seebeck coefficient remained high with delayed bipolar effects. As a result, both the peak in Seebeck coefficient and plateau in power factor ($S^2\sigma$) were shifted to a higher temperature with increased Pb doping, extending the plateau of zT to higher temperatures. As one can see in Figure 4f, our 1% Pb (8.00×10^{19} cm^{-3}) and 1.5% Pb (1.25×10^{20} cm^{-3}) samples are well optimized in terms of carrier concentration to achieve a maximum power factor at 500 and 600 K, respectively.

Besides the tuned power factor, the total thermal conductivity of the nanocomposite is pronouncedly reduced compared to bulk grain materials reported in the literature, and comparable to the κ_{tot} of other nanostructured BiSbTe at room temperature (Figure 5b). Moreover, due to the delayed onset of bipolar conduction in our Pb-doped material, the thermal conductivity remains consistently low over the investigated temperature range, whereas the other studies report a notable increase in κ_{tot} above 400 K (Figure 5b).[8,10] We can model the various contributions to thermal conductivity, as κ_{tot} is expressed as $\kappa_e + \kappa_l + \kappa_{bi}$, in which κ_e is electronic contribution, κ_l is the lattice part, and κ_{bi} is the bipolar thermal conductivity. κ_e is estimated as $L\sigma T$, where L is the Lorenz number (calculated through BTE; Figure S14f, Supporting Information) and σ is the electrical conductivity. We find that the electronic contribution to the κ_{tot} is around 25–40% depending on the doping level (Table S2, Supporting Information).

From the TEM (Figure 3e and the nanograin as indicated by yellow boundaries in Figure S11, Supporting Information) and SEM (Figure S12, Supporting Information) study of PbTe-$Bi_{0.7}Sb_{1.3}Te_3$, both the nanograins of PbTe and $Bi_{0.7}Sb_{1.3}Te_3$ do not grow much in size upon SPS. XRD is also used to estimate the grain size, d, based on the Scherrer equation ($d = K\lambda/\beta\cos\theta$,

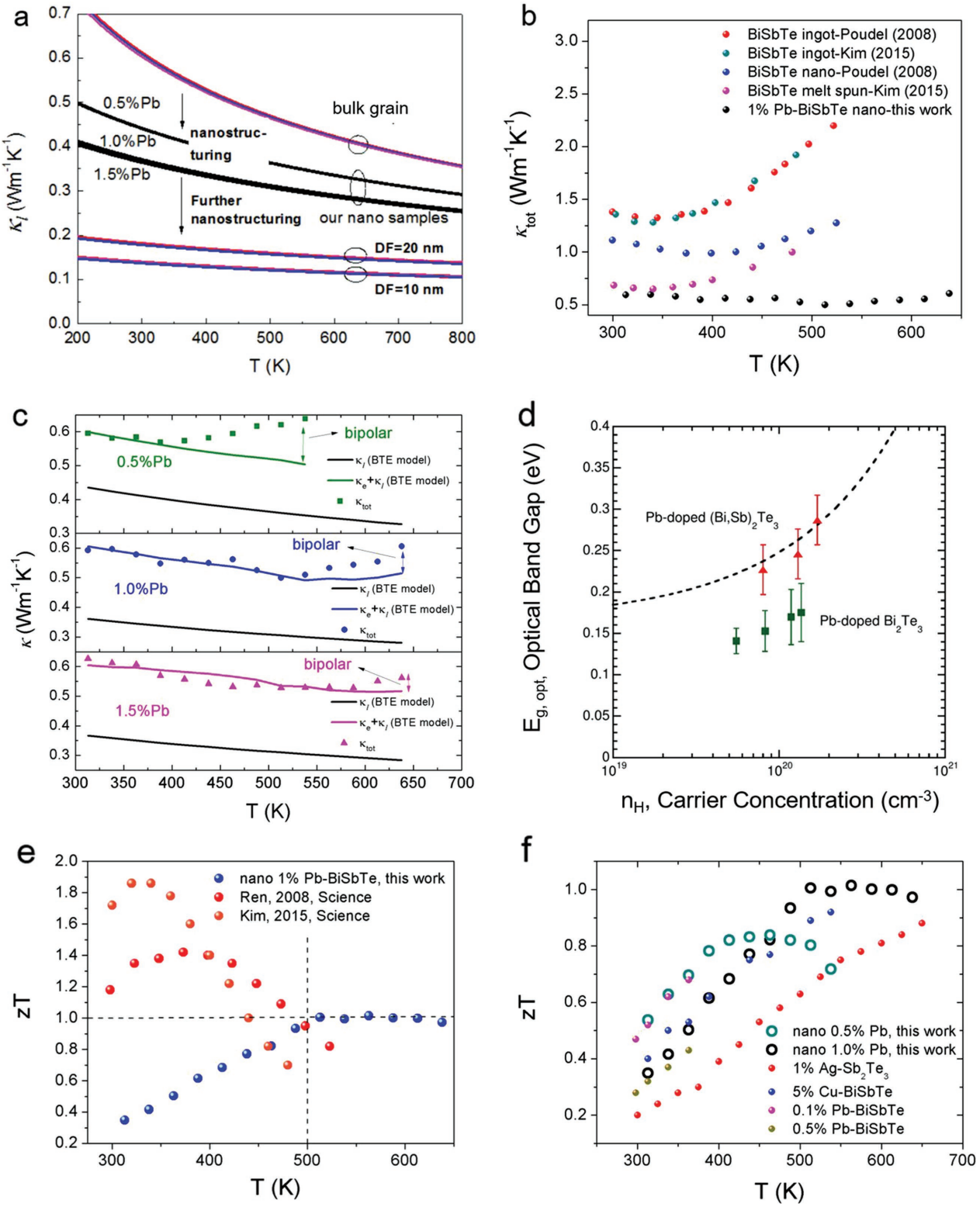

Figure 5. Experimental and theoretical study on the origin of high zT. a) Simulated $\kappa_{lattice}$ as a function of grain diameter (effect of nanostructuring); b) a comparison of κ_{total} of our nano-1.0% Pb-BiSbTe samples with literature values of BiSbTe-based materials;[8,10] c) a breakdown of thermal conductivity: K_l, $K_l + K_e$ and K_{tot}; d) the optical bandgap of select Pb-BiSbTe samples with different carrier concentrations (red triangles), as compared to single parabolic band (SPB)-derived bandgaps (dash line) and the bandgaps of Pb-doped Bi_2Te_3 (green squares);[29] e) the zT of our 1% Pb-doped nanocomposite in comparison with previously reported undoped BiSbTe;[8,10] and f) the zT of our nanocomposites in comparison with doped BiSbTe in the literature (1% Ag-Sb_2Te_3,[16] 5% Cu-$Bi_{0.5}Sb_{1.5}Te_3$,[18] 0.1% and 0.5% Pb-$Bi_{0.4}Sb_{1.6}Te_3$[15]).

Table 1. Band structure and material parameters used in BTE simulations for the electron transport modeling of the Pb-doped $Bi_{0.7}Sb_{1.3}Te_3$ samples at room temperature.

Parameter	0.5% Pb	1.0% Pb	1.5% Pb
Electronic bandgap [eV]		0.22	
Electron effective mass [m_0]		0.63	
Hole effective mass [m_0]		1.19	
Hole concentration [cm^{-3}]	4×10^{19}	8×10^{19}	1.1×10^{20}
Hole mobility [$cm^2\ V^{-1}\ s^{-1}$]	58.6	39.2	32.0

where K is the shape factor (0.9), λ is the X-ray wavelength, β is the full width at half maximum (FWHM, averaged on several peaks), and θ is the Bragg angle, d = 61, 38, and 50 nm for 0.005, 0.010, and 0.015 Pb samples, respectively.[33] The nanosize of the grain is likely to be benefited from the fast (5 min) and efficient sintering process of SPS, as compared to conventional technique such as melt ingot forming and hot pressing. Consequently, κ_l can be strongly reduced in contrast to the bulk-grain counterpart, due to the intensified grain boundary scattering of phonons in our nanocomposites.

This is corroborated by the theoretical modeling of κ_l. Since Bi_2Te_3 and Sb_2Te_3 have three dispersive acoustic branches and many low-energy optical branches, we use a phonon BTE model[34] together with an exact full phonon dispersion obtained from first-principles (density functional theory) calculations[35] rather than a simple Debye model (only one branch with linear dispersion). The total phonon scattering rate for the phonon mode ($\mathbf{k}$,ν) is given by Matthiessen's rule:

$$\frac{1}{\tau_{ph}(\mathbf{k},\nu)} = \frac{1}{\tau_{p}(\mathbf{k},\nu)} + \frac{1}{\tau_{mass}(\mathbf{k},\nu)} + \frac{1}{\tau_{pb}(\mathbf{k},\nu)} + \frac{1}{\tau_{d}(\mathbf{k},\nu)} + \frac{1}{\tau_{b}(\mathbf{k},\nu)} \quad (1)$$

where $\mathbf{k}$ and ν specify the phonon wave vector and dispersion branch, respectively. The terms on the right-hand side are the scattering rates induced by the lattice anharmonicity (p, determined by the pristine Bi_2Te_3 and Sb_2Te_3), Bi-Sb alloy mass disorder (mass, determined by Bi-Sb atomic ratio), Pb impurity (Pb, determined by Pb concentration), other defects (d, including antisites, vacancies, dislocations, distortion, etc., g_{other} as a fitting parameter), and grain boundaries (b, grain diameter DF as a fitting parameter), respectively. Based on the phonon BTE, the lattice thermal conductivity can be calculated by (see the Supporting Information for more details):

$$K_l = \frac{4\pi}{3}\frac{1}{(2\pi)^3}\sum_{\nu}\left[\frac{2}{3}\int_x + \frac{1}{3}\int_z\right]\frac{\hbar^2\omega^2(\mathbf{k},\nu)}{k_B T^2} \times \frac{e^{\frac{\hbar\omega(\mathbf{k},\nu)}{k_B T}}}{\left(e^{\frac{\hbar\omega(\mathbf{k},\nu)}{k_B T}} - 1\right)^2} v^2(\mathbf{k},\nu)\tau(\mathbf{k},\nu)k^2 \mathrm{d}k \quad (2)$$

The only two fitting parameters g_{other} and DF are fitted to best reproduce the low-temperature experimental lattice thermal conductivity when the bipolar effect is negligible. We find that the κ_l of Pb-BiSbTe is mainly determined by the scattering induced by the alloy mass disorder, grain boundaries, and other defects, whereas it is less influenced by the Pb impurity since the Pb concentration is relatively small (Figure S19, Supporting Information). At 300 K, the alloy mass disorder reduces the κ_l of the imaginary mixture of PbTe, Bi_2Te_3, and Sb_2Te_3 from 2.1 W m^{-1} K^{-1} to 0.74 W m^{-1} K^{-1}. The low κ_l achieved in our materials are mainly benefited from the large amounts of defects and small grain sizes. The antisites, vacancies, dislocations, distortion, etc., further reduce κ_l to 0.61 W m^{-1} K^{-1}. The nanograin in 0.005, 0.010, and 0.015 Pb sample reduces it further to 0.442, 0.365, and 0.371 W m^{-1} K^{-1}, respectively (Figure 5a). The lowest value of κ_l (0.365 W m^{-1} K^{-1} at 313 K) reported here is comparable with the lowest reported κ_l (0.31–0.33 W m^{-1} K^{-1} at 300 K) in BiSbTe nanocomposites from the literature, and much lower than that of bulk BiSbTe.[10,20] As indicated in Figure 5a, if the grain size is further reduced to 10–20 nm, κ_l can be reduced to 0.15–0.20 W m^{-1} K^{-1}, which is similar to that of Bi_2Te_3/Sb_2Te_3 superlattices.[36]

The calculated temperature-dependent lattice thermal conductivities are compared to the experimental values in Figure 5c. They match well at low temperatures while they start to deviate from each other at 370, 530, and 570 K for the 0.5%, 1%, and 1.5% Pb-doped BiSbTe nanocomposites, respectively. This indicates that the κ_{bi}, the difference between κ_{tot} and $\kappa_l + \kappa_e$, is suppressed more as the Pb doping concentration increases (Figure 5c). This is in agreement with the temperature-dependent Seebeck data (Figure 4b), and is also the result of the Burstein–Moss shift discussed above, where the optical bandgap increases with increasing carrier concentration (Figure 5d).[37] As a result, the onset temperature of increasing thermal conductivity due to the bipolar effect has been significantly shifted to higher temperatures compared to that of the undoped BiSbTe in the literature (Figure 5b).[8,20]

For our nanocomposite with 1% Pb, the zT reaches 1.0 at 513 K and maintains unity until 613 K, thanks to the optimized $S^2\sigma$ and suppressed κ_l and κ_{bi}. For all previously reported bulk and nanoundoped BiSbTe, the zT drops below 1 for temperatures above 500 K (Figure 5e) due to bipolar contributions to the thermal conductivity (Figure 5b) and Seebeck coefficient (not shown).[8,13,20] For doped-BiSbTe, zT = 1 has also never been achieved in this temperature range (Figure 5f), due to the impaired carrier mobility μ from doping and unreduced κ_l.[15–19] Compared with state-of-the-art undoped BiSbTe, the zT peak of our Pb-BiSbTe nanocomposite is notably shifted to higher temperature, by more than 100 K (Figure 5e). More significantly, in contrast to previously doped BiSbTe materials, the unity plateau of zT lasts from 500 to 600 K, giving a high average value of zT (Figure 5f).

For the low-medium temperature range (500–600 K), which is quite crucial for the recovery of low-grade waste heat, material candidates with $zT > 1$ are extremely limited. GeTe[38] and MgAgSb[39] were found to have decent zT. However, Ge and Ag are precious and rare elements. CdSb[40] and NaPbSbTe[22] are also strong candidates, but use large amounts of toxic elements (Cd, Pb). Doped SnSe single crystals have the best zT along the b-axis,[41] but it is highly anisotropic and fragile, having much lower performance along other crystallographic directions. Our Pb-BiSbTe nanocomposite is based on nanocrystalline

BiSbTe, which is cost-efficient, less toxic (using only 1% Pb), and mechanically rigid. Thus, it can be readily integrated into commercial modules as a p-type leg and can replace the mid-temperature PbTe alloy materials in the 500–600 K range.

In conclusion, we have fabricated tunable PbTe-BiSbTe nanoheterostructures using a scalable, repeatable, wet chemical synthesis method that can be used beyond the field of thermoelectrics. Nanocomposites (≈40 nm grain size) can be made from the nanoheterostructures by spark plasma sintering. The thermoelectric properties were enhanced by tuning the power factor and delaying bipolar conduction through controlled Pb-doping, as well as reducing the lattice thermal conductivity through nanostructuring. These p-type materials have a $zT > 1$ in the low-medium temperature range (513–613 K), making them better than previously reported BiSbTe materials for low grade waste heat recovery.

Supporting Information

Supporting Information is available from the Wiley Online Library or from the author.

Acknowledgements

B.X. and M.T.A. contributed equally to this work. B.X. and Y.W. gratefully acknowledge the support from the startup package provided by Iowa State University and DOE Ames National Lab. M.T.A., T.C.C., and G.J.S. would like to acknowledge funding from the Solid-State Solar-Thermal Energy Conversion Centre (S3TEC), an Energy Frontier Research Centre funded by the U.S. Department of Energy, Office of Science, Basic Energy Sciences under Award No. DE-SC0001299. T.F. and X.R. acknowledge Defense Advanced Research Projects Agency (DARPA) Award No. HR0011-15-2-0037. Y. Z. acknowledges the CSC scholarship and H.Z. thanks DOE BSE Materials Science Division for funding support. M.G.K. thanks the Department of Energy, Office of Science Basic Energy Sciences under grant DE-SC0014520 (thermoelectric, optical measurements).

Received: September 22, 2016
Revised: December 1, 2016
Published online: January 13, 2017

[1] a) G. J. Snyder, E. S. Toberer, *Nat. Mater.* **2008**, *7*, 105; b) W. Liu, X. Yan, G. Chen, Z. Ren, *Nano Energy* **2012**, *1*, 42; c) L.-D. Zhao, V. P. Dravid, M. G. Kanatzidis, *Energy Environ. Sci.* **2014**, *7*, 251.
[2] J. P. Heremans, V. Jovovic, E. S. Toberer, A. Saramat, K. Kurosaki, A. Charoenphakdee, S. Yamanaka, G. J. Snyder, *Science* **2008**, *321*, 554.
[3] Y. Pei, X. Shi, A. LaLonde, H. Wang, L. Chen, G. J. Snyder, *Nature* **2011**, *473*, 66.
[4] Y. Zhang, J.-H. Bahk, J. Lee, C. S. Birkel, M. L. Snedaker, D. Liu, H. Zeng, M. Moskovits, A. Shakouri, G. D. Stucky, *Adv. Mater.* **2014**, *26*, 2755.
[5] L. D. Hicks, M. S. Dresselhaus, *Phys. Rev. B* **1993**, *47*, 16631.
[6] a) J.-S. Rhyee, K. H. Lee, S. M. Lee, E. Cho, S. I. Kim, E. Lee, Y. S. Kwon, J. H. Shim, G. Kotliar, *Nature* **2009**, *459*, 965; b) H. Liu, X. Shi, F. Xu, L. Zhang, W. Zhang, L. Chen, Q. Li, C. Uher, T. Day, G. J. Snyder, *Nat. Mater.* **2012**, *11*, 422.
[7] K. F. Hsu, S. Loo, F. Guo, W. Chen, J. S. Dyck, C. Uher, T. Hogan, E. K. Polychroniadis, M. G. Kanatzidis, *Science* **2004**, *303*, 818.
[8] B. Poudel, Q. Hao, Y. Ma, Y. Lan, A. Minnich, B. Yu, X. Yan, D. Wang, A. Muto, D. Vashaee, X. Chen, J. Liu, M. S. Dresselhaus, G. Chen, Z. Ren, *Science* **2008**, *320*, 634.
[9] K. Biswas, J. He, I. D. Blum, C.-I. Wu, T. P. Hogan, D. N. Seidman, V. P. Dravid, M. G. Kanatzidis, *Nature* **2012**, *489*, 414.
[10] S. I. Kim, K. H. Lee, H. A. Mun, H. S. Kim, S. W. Hwang, J. W. Roh, D. J. Yang, W. H. Shin, X. S. Li, Y. H. Lee, G. J. Snyder, S. W. Kim, *Science* **2015**, *348*, 109.
[11] H. J. Goldsmid, R. W. Douglas, *Br. J. Appl. Phys.* **1954**, *5*, 386.
[12] T. Zhu, L. Hu, X. Zhao, J. He, *Adv. Sci.* **2016**, *3*, 1600004.
[13] H. Goldsmid, *Mater.* **2014**, *7*, 2577.
[14] A. D. LaLonde, Y. Pei, H. Wang, G. Jeffrey Snyder, *Mater. Today* **2011**, *14*, 526.
[15] S. Ganguly, C. Zhou, D. Morelli, J. Sakamoto, C. Uher, S. L. Brock, *J. Solid State Chem.* **2011**, *184*, 3195.
[16] L. P. Hu, T. J. Zhu, X. Q. Yue, X. H. Liu, Y. G. Wang, Z. J. Xu, X. B. Zhao, *Acta Mater.* **2015**, *85*, 270.
[17] W.-T. Chiu, C.-L. Chen, Y.-Y. Chen, *Sci. Rep.* **2016**, *6*, 23143.
[18] J. Cui, W. Xiu, H. Xue, *J. Appl. Phys.* **2007**, *101*, 123713.
[19] Y. Xiao, J.-y. Yang, Q.-h. Jiang, L.-w. Fu, Y.-b. Luo, M. Liu, D. Zhang, M.-y. Zhang, W.-x. Li, J.-y. Peng, F.-q. Chen, *J. Mater. A* **2014**, *2*, 20288.
[20] L.-P. Hu, T.-J. Zhu, Y.-G. Wang, H.-H. Xie, Z.-J. Xu, X.-B. Zhao, *NPG Asia Mater.* **2014**, *6*, e88.
[21] S. Wang, J. Yang, T. Toll, J. Yang, W. Zhang, X. Tang, *Sci. Rep.* **2015**, *5*, 10136.
[22] P. F. P. Poudeu, J. D'Angelo, A. D. Downey, J. L. Short, T. P. Hogan, M. G. Kanatzidis, *Angew. Chem.* **2006**, *118*, 3919.
[23] a) S. W. Finefrock, H. Yang, H. Fang, Y. Wu, *Annu. Rev. Chem. Biomol. Eng.* **2015**, *6*, 247; b) R. J. Mehta, Y. Zhang, C. Karthik, B. Singh, R. W. Siegel, T. Borca-Tasciuc, G. Ramanath, *Nat. Mater.* **2012**, *11*, 233; c) A. Soni, Y. Shen, M. Yin, Y. Zhao, L. Yu, X. Hu, Z. Dong, K. A. Khor, M. S. Dresselhaus, Q. Xiong, *Nano Lett.* **2012**, *12*, 4305.
[24] H. Fang, T. Feng, H. Yang, X. Ruan, Y. Wu, *Nano Lett.* **2013**, *13*, 2058.
[25] H. Yang, J.-H. Bahk, T. Day, A. M. S. Mohammed, G. J. Snyder, A. Shakouri, Y. Wu, *Nano Lett.* **2015**, *15*, 1349.
[26] L. Carbone, P. D. Cozzoli, *Nano Today* **2010**, *5*, 449.
[27] Y. Pei, A. F. May, G. J. Snyder, *Adv. Energy Mater.* **2011**, *1*, 291.
[28] A. Walsh, J. L. F. Da Silva, S.-H. Wei, *Phys. Rev. B* **2008**, *78*, 075211.
[29] a) T. Plecháček, P. Lošťák, J. Navrátil, T. Černohorský, *Cryst. Res. Technol.* **1998**, *33*, 911; b) T. Plecháček, J. Navrátil, J. Horák, P. Lošťák, *Philos. Mag.* **2004**, *84*, 2217.
[30] Z. M. Gibbs, H.-S. Kim, H. Wang, G. J. Snyder, *Appl. Phys. Lett.* **2015**, *106*, 022112.
[31] J.-H. Bahk, A. Shakouri, *Phys. Rev. B* **2016**, *93*, 165209.
[32] C. Jeong, R. Kim, M. Luisier, S. Datta, M. Lundstrom, *J. Appl. Phys.* **2010**, *107*, 023707.
[33] B. E. Warren, *X-Ray Diffraction*, Addison-Wesley Publishing Co, Reading, MA, USA **1969**.
[34] T. Feng, X. Ruan, *J. Nanomater.* **2014**, *2014*, 206370.
[35] V. Chis, I. Y. Sklyadneva, K. A. Kokh, V. A. Volodin, O. E. Tereshchenko, E. V. Chulkov, *Phys. Rev. B* **2012**, *86*, 174304.
[36] R. Venkatasubramanian, E. Siivola, T. Colpitts, B. O'Quinn, *Nature* **2001**, *413*, 597.
[37] M. G. Zachary, L. Aaron, G. J. Snyder, *New J. Phys.* **2013**, *15*, 075020.
[38] E. Hazan, O. Ben-Yehuda, N. Madar, Y. Gelbstein, *Adv. Energy Mater.* **2015**, *5*, 1500272.
[39] H. Zhao, J. Sui, Z. Tang, Y. Lan, Q. Jie, D. Kraemer, K. McEnaney, A. Guloy, G. Chen, Z. Ren, *Nano Energy* **2014**, *7*, 97.
[40] S. Wang, J. Yang, L. Wu, P. Wei, J. Yang, W. Zhang, Y. Grin, *Chem. Mater.* **2015**, *27*, 1071.
[41] L.-D. Zhao, G. Tan, S. Hao, J. He, Y. Pei, H. Chi, H. Wang, S. Gong, H. Xu, V. P. Dravid, C. Uher, G. J. Snyder, C. Wolverton, M. G. Kanatzidis, *Science* **2016**, *351*, 141.

ADVANCED MATERIALS

Supporting Information

for *Adv. Mater.*, DOI: 10.1002/adma.201605140

Nanocomposites from Solution-Synthesized PbTe-BiSbTe Nanoheterostructure with Unity Figure of Merit at Low-Medium Temperatures (500–600 K)

Biao Xu, Matthias T. Agne, Tianli Feng, Thomas C. Chasapis, Xiulin Ruan, Yilong Zhou, Haimei Zheng, Je-Hyeong Bahk, Mercouri G. Kanatzidis, Gerald Jeffrey Snyder,* and Yue Wu**

Supporting Information

Nanocomposites from Solution-Synthesized PbTe-BiSbTe Nano-Heterostructure with Unity Figure of Merit at the Low-Medium Temperatures (500-600 K)

Biao Xu[1]|, Matthias T. Agne[2]|, Tianli Feng[3], Thomas C. Chasapis[2], Xiulin Ruan[3], Yilong Zhou[4], Haimei Zheng[4], Je-Hyeong Bahk[5*], Mercouri G. Kanatzidis[6], G. Jeffrey Snyder[2]*, Yue Wu[1]*.

| These authors contributed equally to this work.

*e-mail: J. H. B, bahkjg@uc.edu, G. J. S, jeff.snyder@northwestern.edu, Y. W., yuewu@iastate.edu

1. Department of Chemical and Biological Engineering, Iowa State University, Ames, Iowa, 50011, USA
2. Department of Materials Science and Engineering, Northwestern University, Evanston, Illinois, 60208, USA
3. Department of Mechanical Engineering, Purdue University, West Lafayette, Indiana, 47907, USA
4. Lawrence Berkeley National Laboratory, Materials Sciences Division, Building 62 Room 211, 1 Cyclotron Road, Berkeley, California, 94720, USA
5. Department of Mechanical and Materials Engineering, University of Cincinnati, Cincinnati, Ohio, 45221, USA
6. Department of Chemistry, Northwestern University, Evanston, Illinois, 60208, USA

Methods

Reagents

Tellurium dioxide (TeO_2, 99.995%), potassium hydroxide (KOH, 99.99%), polyvinylpyrrolidone (PVP, M_w = 40,000), lead acetate trihydrate ($Pb(CH_3COO)_2 \cdot 3H_2O$, 99.99%), bismuth nitrate pentahydrate ($Bi(NO_3)_3 \cdot 5H_2O$, 99.99%), antimony acetate ($Sb(CH_3COO)_3$, 99.99%), hydrazine hydrate aqueous solution ($N_2H_4 \cdot H_2O$, 78-82%), anhydrous hydrazine (N_2H_4, 98%) and ethylene glycol (EG, 99%) are purchased from Sigma-Aldrich. Deionized water and absolute ethanol are used for centrifugation.

Synthesis of 0.01 PbTe – BiSbTe

First, 49.5 mmol (7.9002 g) of TeO_2, 660 mmol (37.026 g) of KOH and 9.9 g of PVP (M_w = 40,000) are dissolved into 495 mL of ethylene glycol (EG). The solution is heated to 100^{o}C and then 8.25 mL of hydrazine hydrate solution (80%) is injected. It turns into dark blue slurry and is kept at 100^{o}C for 1 hour before the temperature is raised to 110^{o}C. In the second step, the stock solution of lead acetate trihydrate (0.495 mmol (0.1877 g) of $Pb(OAc)_2 \cdot 3H_2O$ in 27.5 mL of EG) is added dropwise into the hot dispersion of Te nanowire. Then another 1 hour of heating is maintained for the formation of PbTe-Te nanoheterostructure. Finally, the ethylene glycol solution (88 mL) of Bi and Sb (8.1675 mmol (3.9717 g) of $Bi(NO_3)_3 \cdot 5H_2O$ and 24.5025 mmol (7.3236 g) of $Sb(OAc)_3$) is heated to 160^{o}C on a hot plate and then added in drop by drop, with precedent injection of anhydrous hydrazine (14.3 mL, N_2H_4) assisting the reduction of Bi and Sb. The whole slurry is heated at 110^{o}C for 1 hour and then incubated at 140^{o}C for another 8 hours before the production of PbTe-BiSbTe nanoheterostructure. After synthesis, the product is washed and centrifuged using deionized water for 3 times and then absolute ethanol for 2 times.

Synthesis of 0.005 PbTe-BiSbTe, 0.015 PbTe-BiSbTe

Every step is the same as those of 0.01 PbTe – BiSbTe except the amount of Pb, Bi and Sb.

For 0.005 Pb sample, the amounts are: 0.2475 mmol (0.0938 g) of $Pb(OAc)_2 \cdot 3H_2O$, 8.2088 mmol (3.9818 g) of $Bi(NO_3)_3 \cdot 5H_2O$ and 24.6262 mmol (7.3605 g) of $Sb(OAc)_3$).

For 0.015 Pb sample, the amounts are: 0.7425 mmol (0.2816 g) of $Pb(OAc)_2 \cdot 3H_2O$, 8.1262 mmol (3.9419 g) of $Bi(NO_3)_3 \cdot 5H_2O$ and 24.3788 mmol (7.2866 g) of $Sb(OAc)_3$).

Removing surfactant

The product from solution synthesis is washed with water and centrifuged for three times. Then the precipitate is re-dispersed in an 8% (v/v) ethanol solution of hydrazine hydrate and stirred for 24 hours to strip off the surface-bound PVP. After that, the dispersion is washed with ethanol for another 3 times. Then the paste is vacuum-pumped overnight to yield dry solid. The dried solid is about 9.6 gram.

Characterizations

X-ray diffraction (XRD) is recorded on a Rigaku Ultima U4, with Cu Kα radiation (λ = 1.5418 Å), at 40 kV and 44 mA. Transmission Electron Microscopy (TEM) is acquired on a JEOL 2100F at 200 kV and a FEI G-20 TEM at 200 kV. Scanning Electron Microscopy (SEM) is conducted on a FEI Quanta 250, with Energy Dispersion Spectra (EDS). Optical band gap is measured in 0-0.7 eV with a Nicolet 6700 FT-IR spectrometer.

Thermoelectric properties

The samples are placed between a cold and a hot end while the temperature gradient and the electrical voltage across the two ends are simultaneously measured to calculate the Seebeck coefficients (S) in a Linseis LSR-3. The electrical conductivity (σ) is measured in a Linseis LSR-3 using a four-probe configuration and re-confirmed using a Van der-Pauw method in Northwestern University. The thermal conductivity (κ) is expressed as $\kappa = D_T \cdot C_p \cdot \rho$. Thermal diffusivity ($D_T$) is measured using laser flash method in a Linseis XFA 600. Specific Heat (C_p) is measured on a Linseis DSC using sapphire as the standard. Mass density (ρ) is calculated from the sample mass and dimensions. Hall coefficients (R_H) and resistivity (ρ) (Van der Pauw, 4-point probe) were measured simultaneously with a home-built instrument

(Northwestern University) using a 2 T magnet with pressure-assisted Molybdenum contacts. The deviation of *S* is around 2%, electrical conductivity σ (5%) and κ (5%). The combined uncertainty of zT ($S^2\sigma T/\kappa$) is around 15%.

Characterizations of the intermediate product of nanoheterostructure

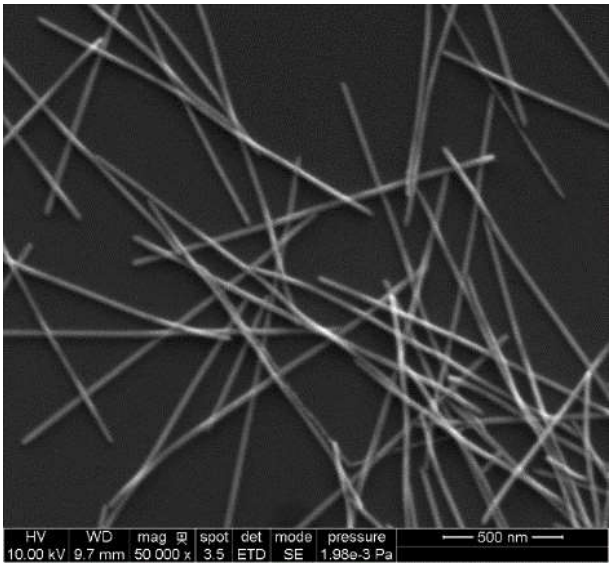

Figure S1. SEM image of Te nanowire in the 1st step of synthesis.

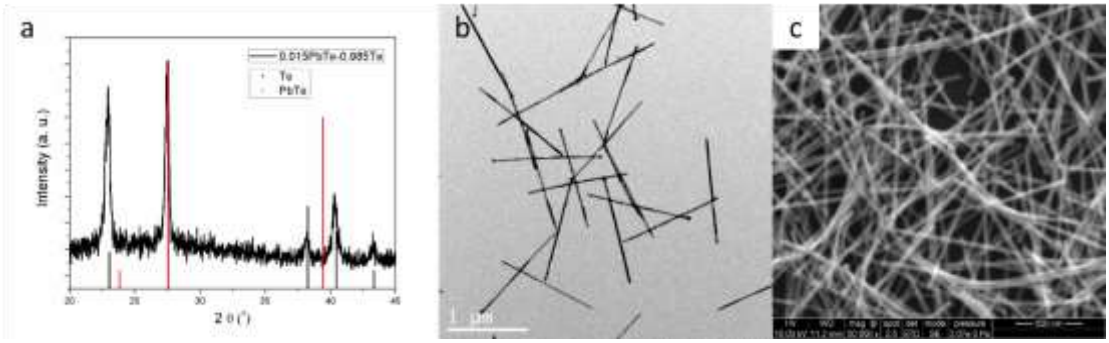

Figure S2. a) XRD pattern, b) TEM image and c) SEM image of 1.5% PbTe-Te in the 2nd step of synthesis.

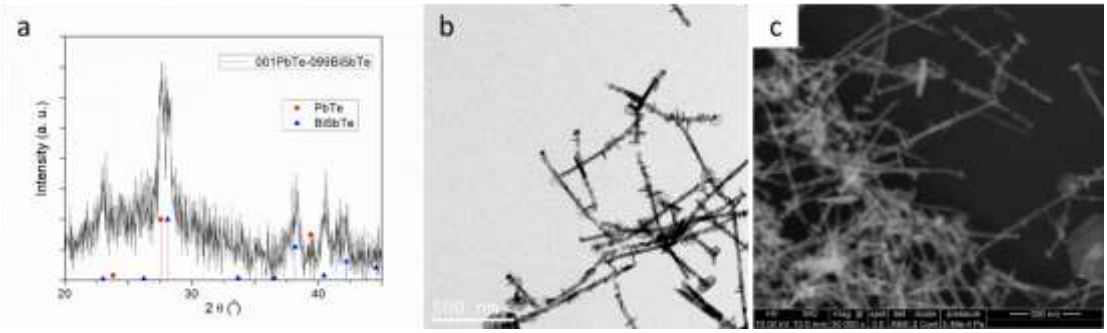

Figure S3. a) XRD pattern, b) TEM image and c) SEM image of 1% PbTe-BiSbTe in the 3rd step of synthesis.

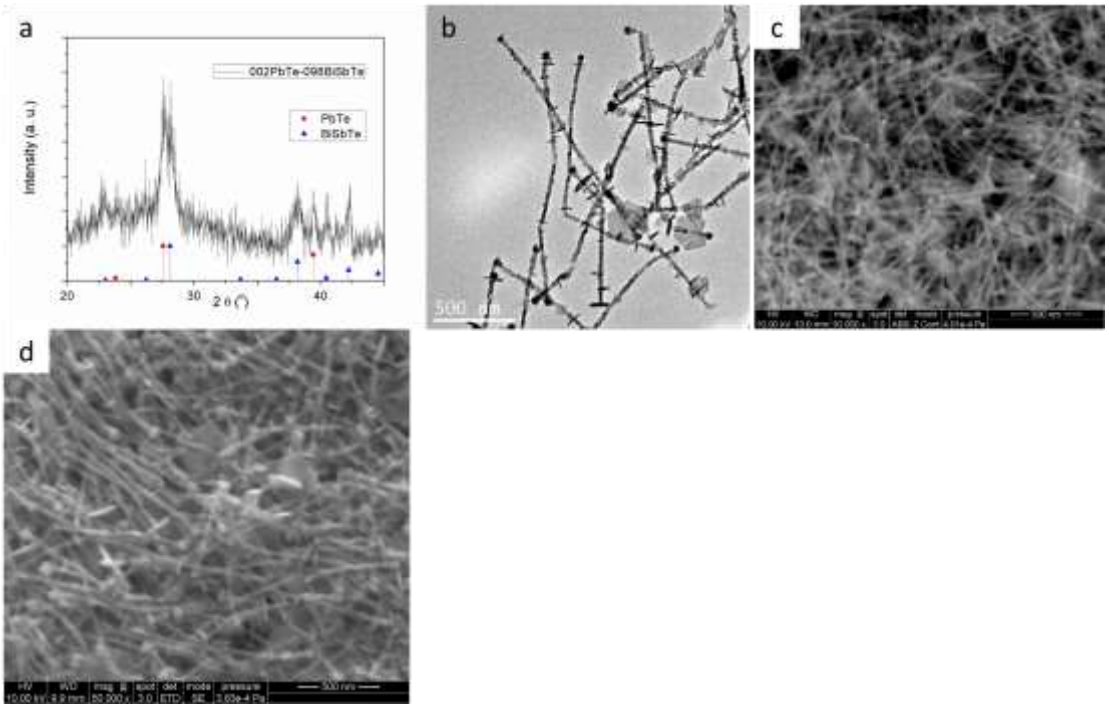

Figure S4. a) XRD pattern, b) TEM image and c) SEM image of 2% PbTe-BiSbTe in the 3rd step of synthesis, d) SEM image of 4% PbTe-BiSbTe.

Atomic Structures

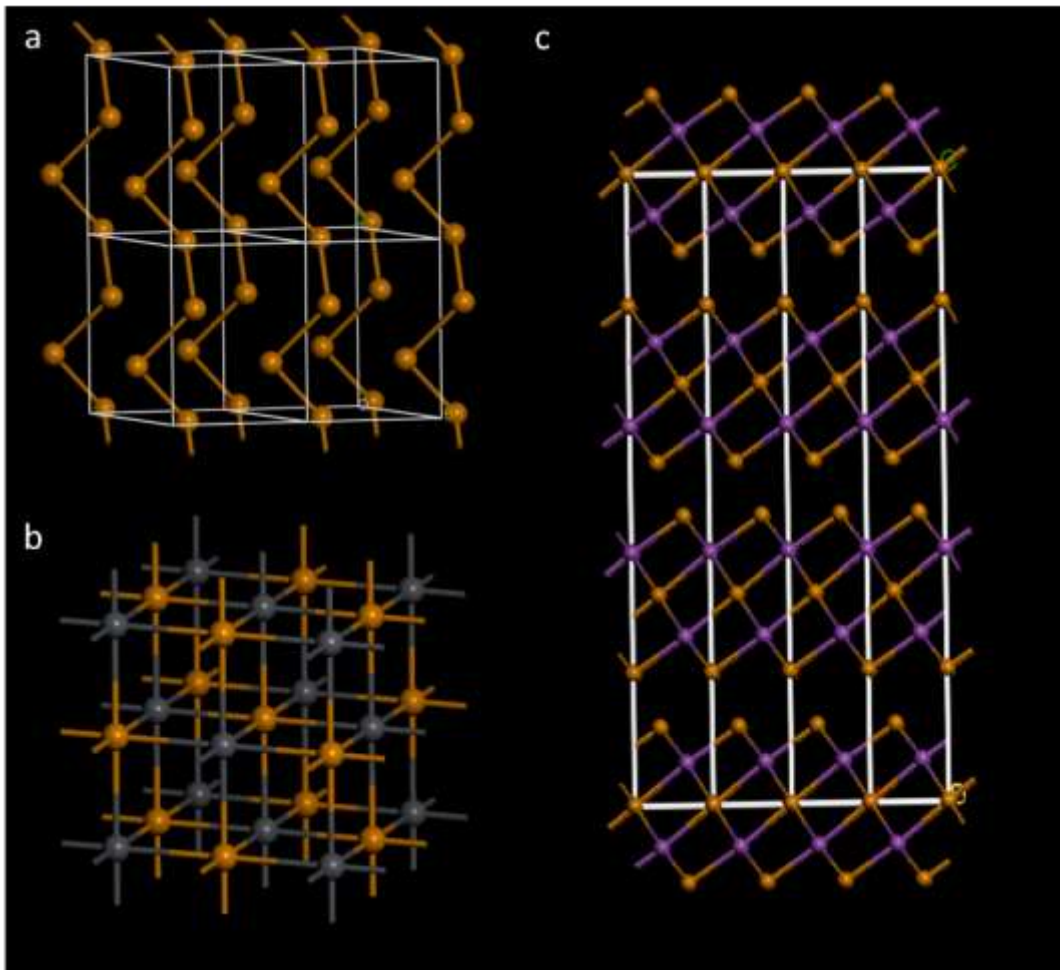

Figure S5. crystal structure of a) Te, b) PbTe and c) $Bi_xSb_{2-x}Te_3$.

The crystal structure of Te is constructed according to:

_publ_section_title 'The crystal structure of tellurium'

_journal_coden_ASTM PHMAA4

_journal_name_full 'Philosophical Magazine, Serie 6 (1901-1925)'

_journal_page_first 477

_journal_page_last 496

_journal_volume 48

_journal_year 1924

_chemical_compound_source synthetic

_chemical_formula_structural Te

_chemical_formula_sum Te

_chemical_name_common Tellurium

_chemical_name_mineral Tellurium

_chemical_name_systematic Tellurium

_space_group_IT_number 152

_symmetry_cell_setting trigonal

_symmetry_Int_Tables_number 152

_symmetry_space_group_name_Hall 'P 31 2"'

_symmetry_space_group_name_H-M 'P 31 2 1'

_cell_angle_alpha 90

_cell_angle_beta 90

_cell_angle_gamma 120

_cell_formula_units_Z 3

_cell_length_a 4.454

_cell_length_b 4.454

_cell_length_c 5.924

_cell_volume 101.8

_exptl_crystal_density_meas 6.31(8)

_atom_site_label _atom_site_type_symbol _atom_site_fract_x _atom_site_fract_y

_atom_site_fract_z _atom_site_occupancy _atom_site_U_iso_or_equiv

Te1 Te0 3 a 0.269 0. 0.3333 1. 0 d

The crystal structure of PbTe is constructed according to:

_journal_name_full

'Zeitschrift fuer Physikalische Chemie (Frankfurt Am Main)'

_journal_page_first 145

_journal_page_last 155

_journal_volume 144

_journal_year 1985

_chemical_formula_sum 'Pb Te'

_chemical_name_systematic 'Pb Te'

_space_group_IT_number 225

_symmetry_space_group_name_Hall '-F 4 2 3'

_symmetry_space_group_name_H-M 'F m -3 m'

_cell_angle_alpha 90

_cell_angle_beta 90

_cell_angle_gamma 90

_cell_formula_units_Z 4

_cell_length_a 6.462

_cell_length_b 6.462

_cell_length_c 6.462

_cell_volume 269.837

_citation_journal_id_ASTM ZPCFAX

_cod_data_source_file Leute_ZPCFAX_1985_1367.cif

_cod_data_source_block Pb1Te1

_cod_original_cell_volume 269.8366

_cod_chemical_formula_sum_orig 'Pb1 Te1'

_atom_site_label _atom_site_type_symbol _atom_site_fract_x _atom_site_fract_y

_atom_site_fract_z _atom_site_occupancy _atom_site_U_iso_or_equiv

Te1 Te 0.5 0.5 0.5 1 0.0

Pb1 Pb 0 0 0 1 0.0

The crystal structure of $Bi_xSb_{2-x}Te_3$ is drawn according to:

_journal_name_full

'Izvestiya Akademii Nauk SSSR, Neorganicheskie Materialy'

_journal_page_first 1090

_journal_page_last 1094

_journal_volume 6

_journal_year 1970

_chemical_formula_sum 'Bi0.4 Sb1.6 Te3'

_chemical_name_systematic '(Bi0.2 Sb0.8)2 Te3'

_space_group_IT_number 166

_symmetry_space_group_name_Hall '-R 3 2"'

_symmetry_space_group_name_H-M 'R -3 m :H'

_cell_angle_alpha 90

_cell_angle_beta 90

_cell_angle_gamma 120

_cell_formula_units_Z 3

_cell_length_a 4.3

_cell_length_b 4.3

_cell_length_c 30.28

_cell_volume 484.868

_citation_journal_id_ASTM IVNMAW

_cod_data_source_file Stasova_IVNMAW_1970_516.cif

_cod_data_source_block Bi0.4Sb1.6Te3

_cod_original_cell_volume 484.8679

_atom_site_label _atom_site_type_symbol _atom_site_fract_x _atom_site_fract_y _atom_site_fract_z _atom_site_occupancy _atom_site_U_iso_or_equiv

Te1 Te-2 0 0 0 1 0.0

Bi1 Bi+3 0 0 0.398 0.2 0.0

Sb1 Sb+3 0 0 0.398 0.8 0.0

Te2 Te-2 0 0 0.2115 1 0.0

Then we cleave the typical crystal planes that are observed in HRTEM, such as Te (001), PbTe (111) and $Bi_xSb_{2-x}Te_3$ (001) (Figure S6).

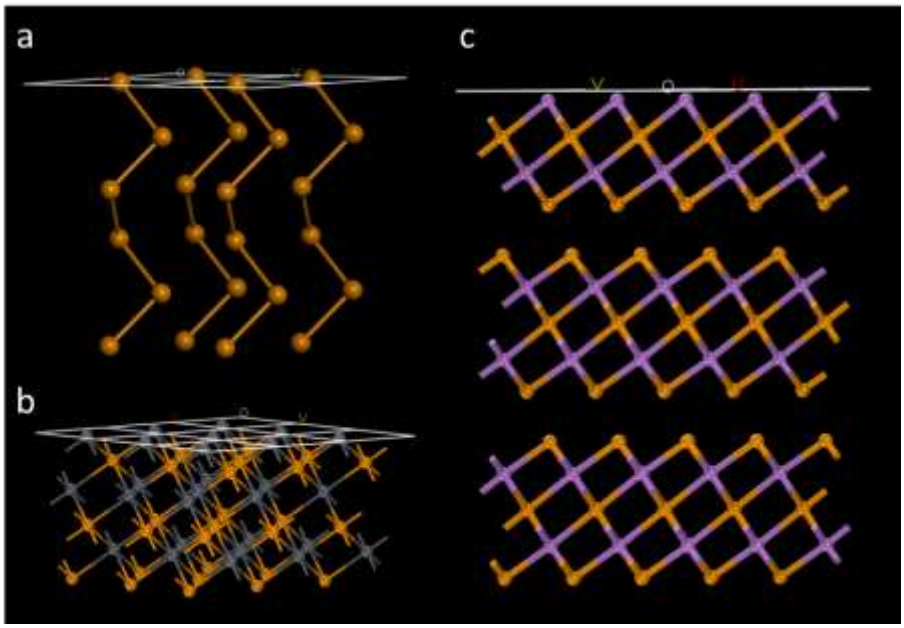

Figure S6. Atomistic structure of a) Te (001), b) PbTe (111) and c) $Bi_xSb_{2-x}Te_3$ (001)

We find that in these planes, the interatomic distance between Te-Te (4.454 Å), Pb-Pb (4.569 Å) and Bi-Bi (4.300 Å) match quite well with each other. Therefore, we have tried to construct the Te (001)-PbTe (111), Te (001)-$Bi_xSb_{2-x}Te_3$ (001) and PbTe (111)-$Bi_xSb_{2-x}Te_3$ (001) interfaces. These interfaces are observed in the HRTEM (Figure 2 in the main text).

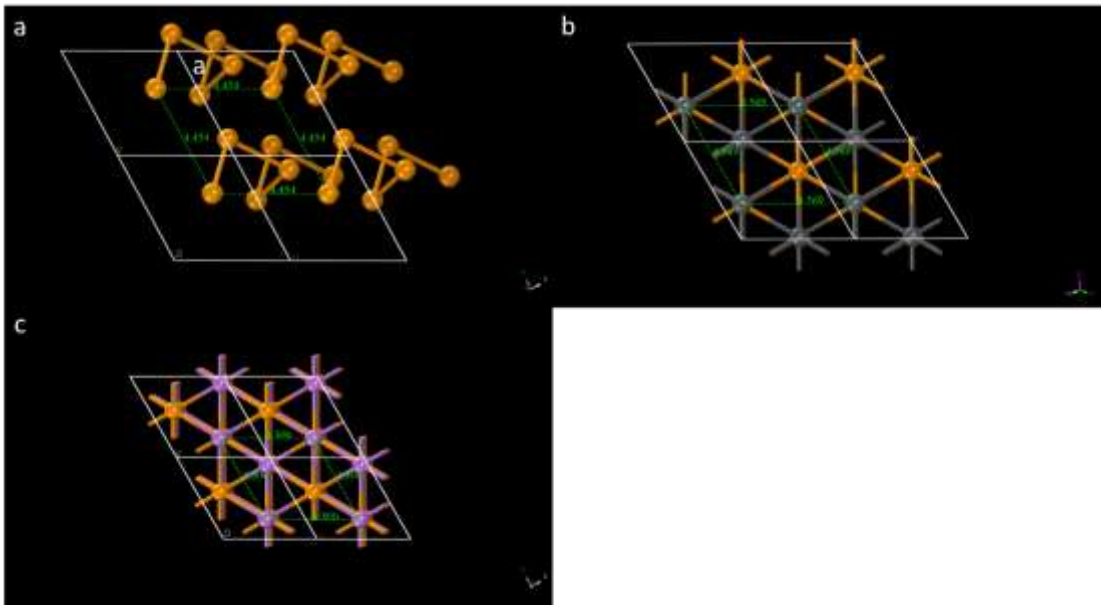

Figure S7. Interatomic distances in a) Te (001) surface, b) PbTe (111) surface, c) $Bi_xSb_{2-x}Te_3$ (001) surface.

In the PbTe (111)-Te (001) interface, the surface Pb 3c atom in the PbTe (111) slab is saturated by 3 Te atoms, completing the d^2sp^3 octahedral coordination. The surface Te (001) 1c atom is saturated by 3 Pb atoms.

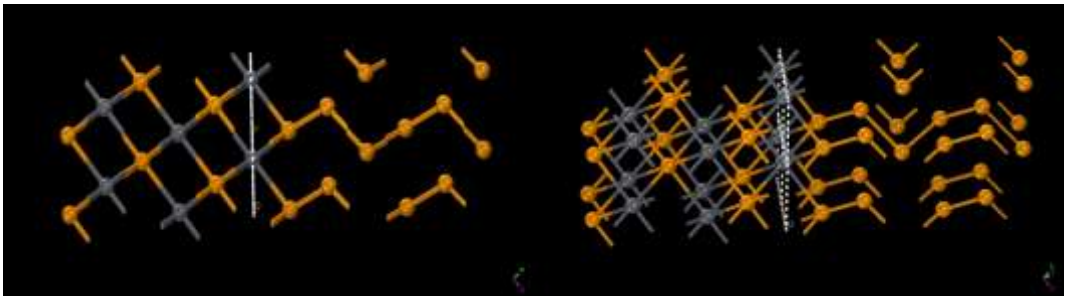

Figure S8. PbTe (111)-Te (001) interface

In the $Bi_xSb_{2-x}Te_3$ (001)-Te (001) interface, the surface Bi(Sb) 3c atom in the $Bi_xSb_{2-x}Te_3$ (001) slab is saturated by 3 Te atoms, completing the d^2sp^3 octahedral coordination. The surface Te (001) 1c atom is saturated by 3 Bi(Sb) atoms.

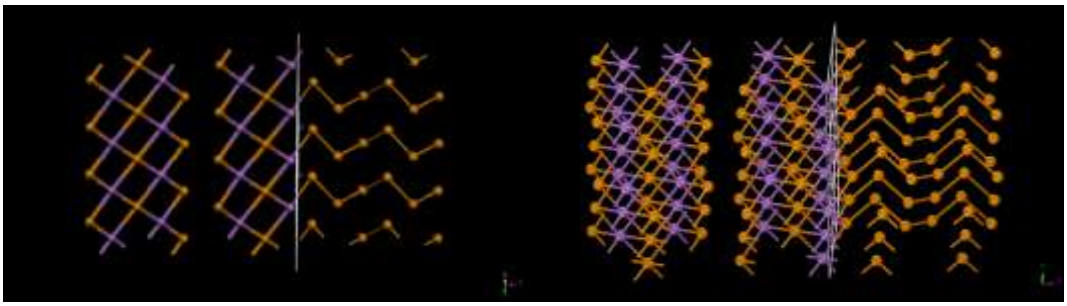

Figure S9. $Bi_xSb_{2-x}Te_3$ (001)-Te (001) interface

In the $Bi_xSb_{2-x}Te_3$ (001)-PbTe (111) interface, the surface Bi(Sb) 3c atom in the $Bi_xSb_{2-x}Te_3$ (001) slab is saturated by 3 Te atoms, completing the d^2sp^3 octahedral coordination. The surface Te 3c atom in the PbTe (111) slab is saturated by 3 Bi(Sb) atoms, completing the d^2sp^3 octahedral coordination.

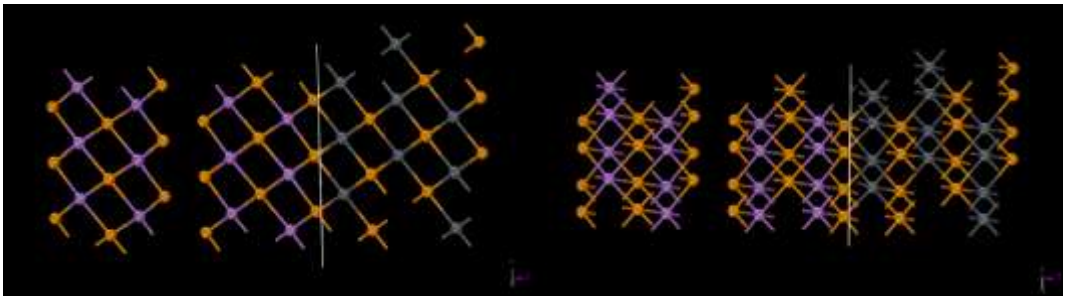

Figure S10. $Bi_xSb_{2-x}Te_3$ (001)-PbTe (111) interface

Characterizations of after-SPS nanocomposite

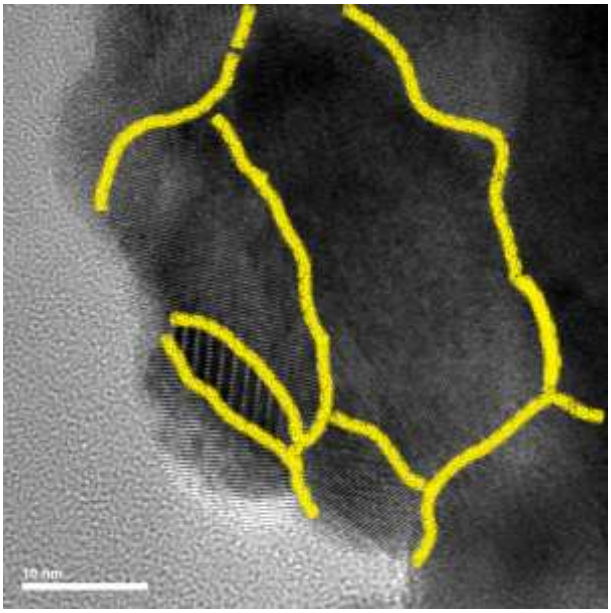

Figure S11. HRTEM image of 0.01 Pb-BiSbTe disk (after SPS), the yellow lines define the grain boundary.

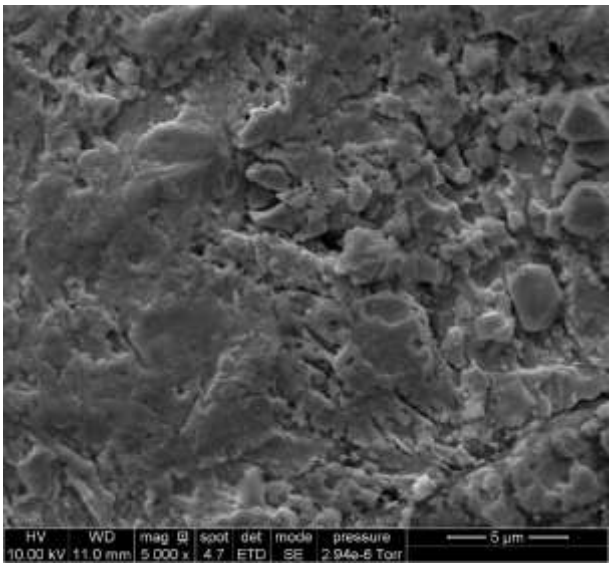

Figure S12. SEM image of 0.01 Pb-BiSbTe disk (after SPS)

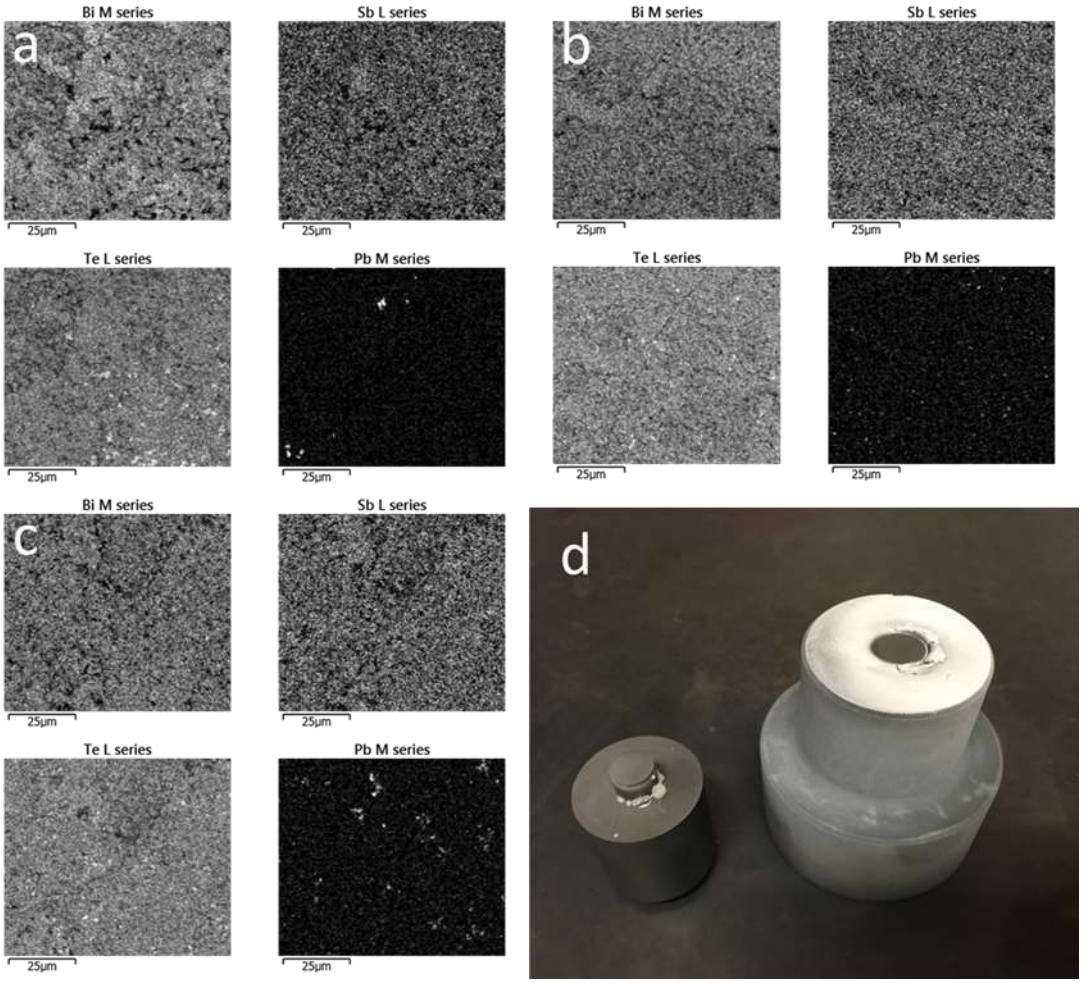

Figure S13. SEM EDS elemental mapping of a) 0.01 Pb – BiSbTe, b) 0.02 Pb – BiSbTe and c) 0.04 Pb – BiSbTe samples (after SPS). d) Digital image of the expelled Te on the graphite die and spacer.

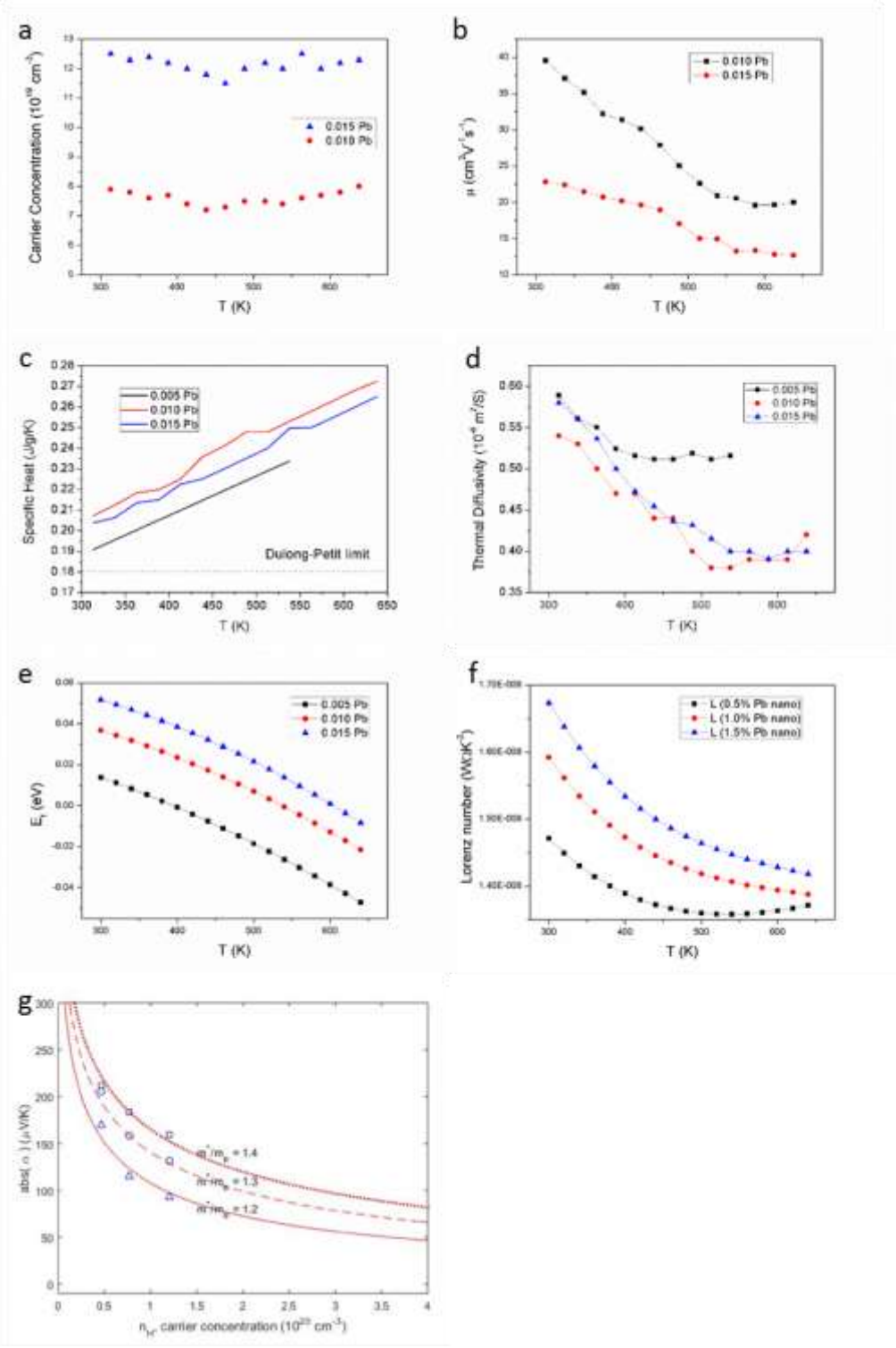

Figure S14. a) carrier concentration, b) carrier mobility, c) specific heat, d) thermal diffusivity, e) fermi level, f) Lorenz number and g) Pisarenko plot (using single parabolic band model) of different samples at T = 313 K (blue triangles), 413 K (blue circles), and 488 K (blue squares).

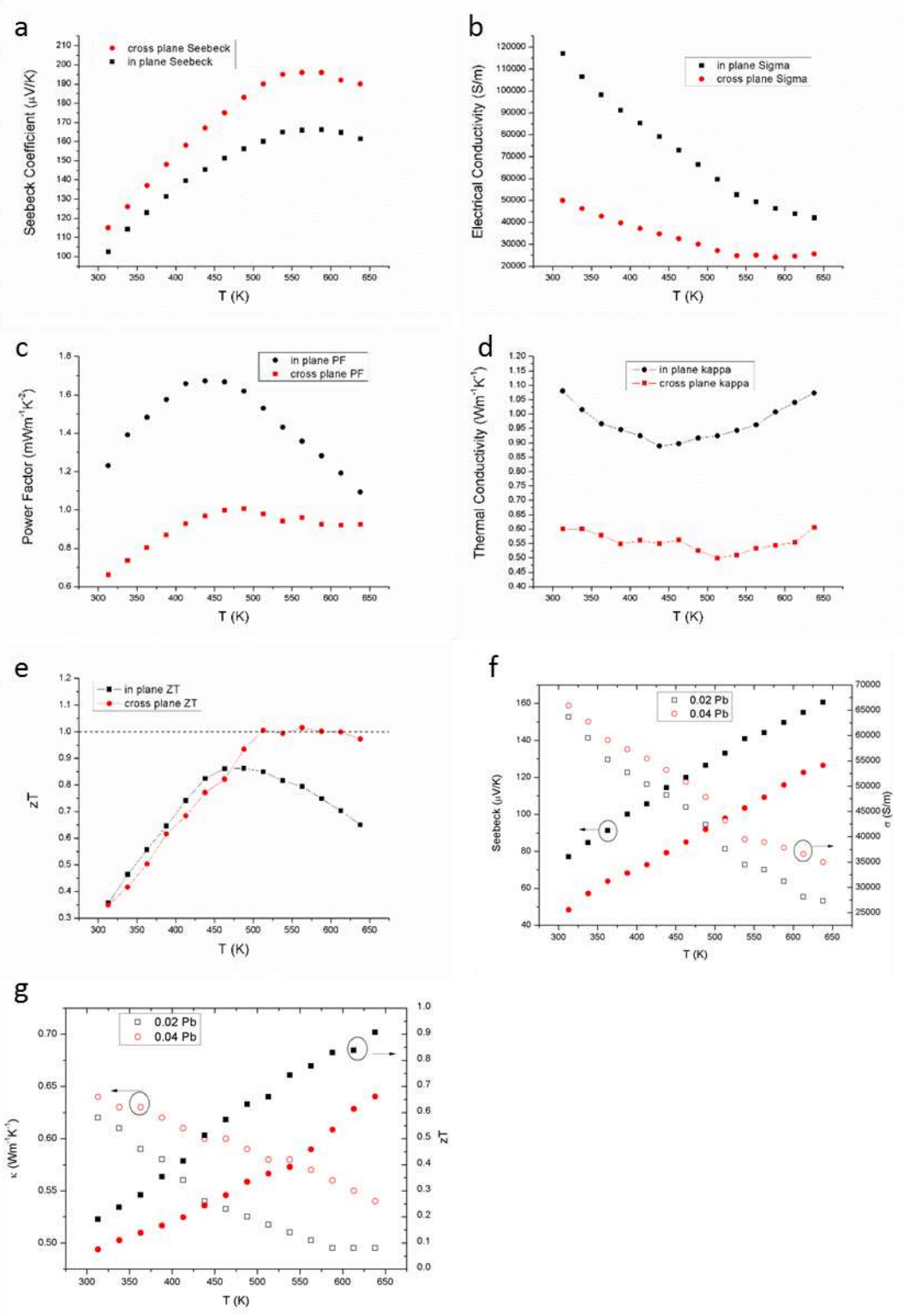

Figure S15. In-plane measurement vs cross-plane measurement of a) Seebeck coefficient, b) electrical conductivity, c) power factor, d) thermal conductivity and e) figure of merit of 0.01 Pb-BiSbTe sample, f) Seebeck coefficient (solid markers) and electrical conductivity (void

markers) of 0.02 Pb (black) and 0.04 Pb (red) samples, g) thermal conductivity (void markers) and zT (solid markers) of 0.02 Pb (black) and 0.04 Pb (red) samples.

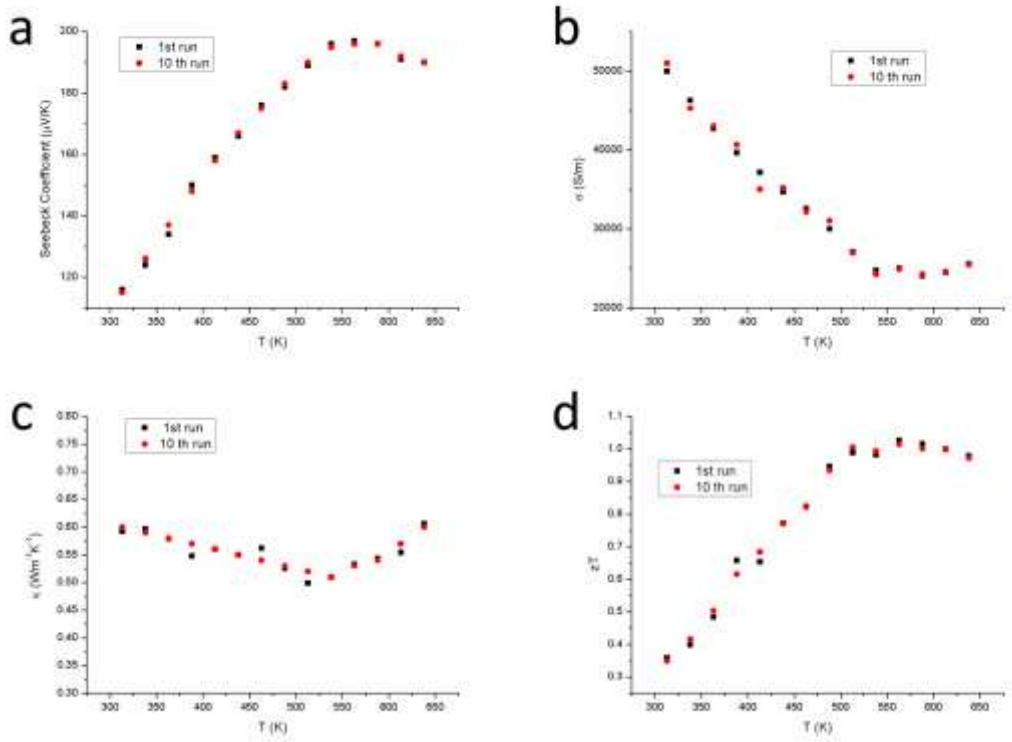

Figure S16. Thermal stability of 0.01 Pb-BiSbTe sample. a) Seebeck coefficient, b) electrical conductivity, c) thermal conductivity and d) zT in the 1st run (black) and 10th run (red).

Band Gap Measurements

Table S1. Goldsmid-Sharp gap calculations for Pb-doped BST

Nominal Pb concentration (%)	S_{max} (μV/K)	T_{max} (K)	E_g (eV)
0.5	218.1	489.7	0.214
1.0	196.4	577.5	0.227
1.5	184.3	630.2	0.232

The optical band gap was determined from the diffuse reflectance results of Fourier transform infrared (FT-IR) spectroscopy. The leading side of the absorption peak was fit by a power law equation. An example of the FT-IR data and the power law fit is shown in Fig. S17a. The power law fit was then subtracted from the FT-IR data to remove the free carrier contribution to absorption. Two standard methods of plotting the data were used to determine the gap (Fig. S18), the difference in the two methods is 30 meV. The SPB model for optical band gap vs carrier concentration is given by (see main text for more discussion): $E_g = E_{g0} + (\hbar^2/2m^*)(3\pi n)^{2/3}$. Furthermore, the optical band gap is plotted for nominal Pb concentrations (Fig. S18b). As it is debated whether BiSbTe materials are direct or indirect band gap semiconductors, we show the calculations assuming each condition. Also shown is the Goldsmid-Sharp gap (Table S1 and blue circles in Fig. S17b), a type of transport band gap, calculated from the temperature dependent Seebeck data through the semi-empirical relation: $E_g = 2eS_{max}T_{max}$, where e is the electric charge.

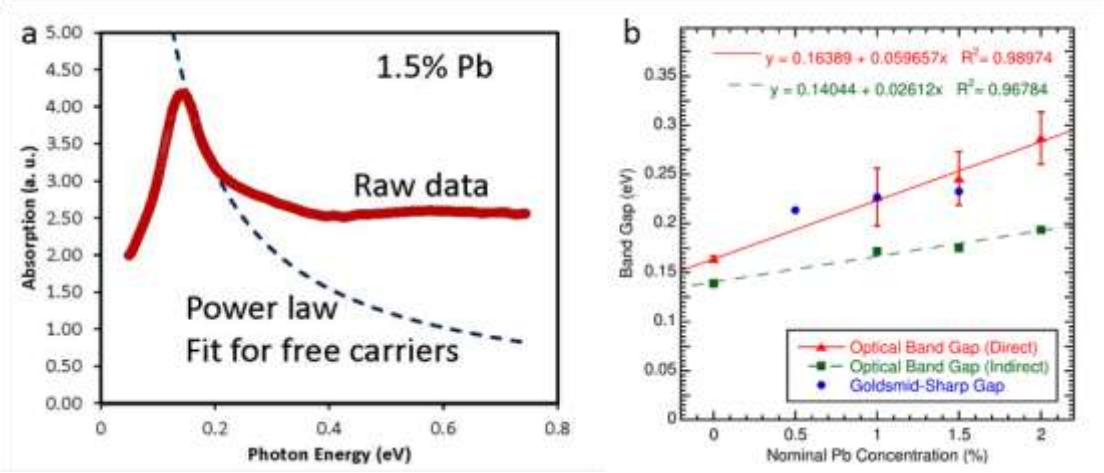

Figure S17 a) Typical optical absorption data from FT-IR measurements. Also shown is the power law fit through the leading side of the absorption peak, b) experimental optical gaps, assuming direct (red triangles) and indirect transitions (green squares), determined from FT-IR data compared with the Goldsmid-Sharp gap calculated from Seebeck data (blue spheres).

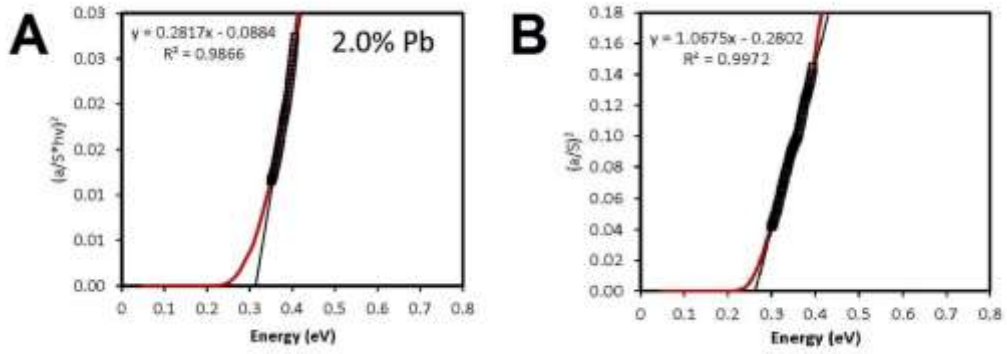

Figure S18 After subtraction of the free carrier contribution to absorption, the data (for all compositions, but only 2% Pb composition is shown) was plotted in two standard ways: a) $(\alpha h\nu)^2$ vs energy, and b) α^2 vs energy.

Thermal Conductivity Modeling

Phonon Boltzmann transport equation model

The total phonon scattering rate for the phonon mode ($\mathbf{k}, \nu$) is given by Matthiessen's rule,

$$\frac{1}{\tau_{ph}(\mathbf{k},\nu)} = \frac{1}{\tau_{p}(\mathbf{k},\nu)} + \frac{1}{\tau_{mass}(\mathbf{k},\nu)} + \frac{1}{\tau_{Pb}(\mathbf{k},\nu)} + \frac{1}{\tau_{d}(\mathbf{k},\nu)} + \frac{1}{\tau_{b}(\mathbf{k},\nu)}, \quad \text{(S1)}$$

where $\mathbf{k}$ and ν specify the phonon wave vector and dispersion branch, respectively. The terms on the right hand side are the scattering rates induced by the lattice anharmonicity, Bi-Sb alloy mass disorder, Pb impurity, other defects, and grain boundaries, respectively. They are calculated by

$$\frac{1}{\tau_{p}(\mathbf{k},\nu)} = \frac{Ak_{B}T}{M_{a}v^{2}(\mathbf{k},\nu)} \frac{\gamma^{2}\omega^{2}(\mathbf{k},\nu)}{\omega_{\max}(\nu)} \exp\left(-\frac{\hbar\omega_{\max}(\nu)}{3k_{B}T}\right). \quad \text{(S2)}$$

$$\frac{1}{\tau_{mass}(\mathbf{k},\nu)} = \frac{\pi}{2} g_{mass}\omega^{2}(\mathbf{k},\nu)DOS(\omega). \quad \text{(S3)}$$

$$\frac{1}{\tau_{Pb}(\mathbf{k},\nu)} = \frac{\pi}{2} g_{Pb}\omega^{2}(\mathbf{k},\nu)DOS(\omega). \quad \text{(S4)}$$

$$\frac{1}{\tau_{d}(\mathbf{k},\nu)} = \frac{\pi}{2} g_{other}\omega^{2}(\mathbf{k},\nu)DOS(\omega). \quad \text{(S5)}$$

$$\frac{1}{\tau_{b}(\mathbf{k},\nu)} = \frac{v(\mathbf{k},\nu)}{DF}. \quad \text{(S6)}$$

For the phonon-phonon scattering[1] in Eq. (S2), $\omega(\mathbf{k},\nu)$ and $v(\mathbf{k},\nu)$ and are the spectral phonon frequency and velocity, respectively. $\omega_{max}(\nu)$ is the maximum frequency of the phonon branch ν. γ is the Grüneisen parameter with the values 1.5 and 1.7 for Bi_2Te_3 and Sb_2Te_3, respectively[2]. M_a is the average atomic mass, given by

$$M_a = \frac{\alpha_{Pb}M_{Pb} + \alpha_{Bi}M_{Bi} + \alpha_{Sb}M_{Sb} + \alpha_{Te}M_{Te}}{\alpha_{Pb} + \alpha_{Bi} + \alpha_{Sb} + \alpha_{Te}}, \quad \text{(S7)}$$

where α is the stoichiometric coefficient. The values of coefficient A, 0.83 and 0.66 for Bi_2Te_3 and Sb_2Te_3 respectively, are determined by the experimental room temperature lattice thermal conductivities values 1.6 W/mK and 2.4 W/mK for pure Bi_2Te_3 and Sb_2Te_3, respectively[3].

For the mass disorder, impurity and defect scattering[4] in Eqns. (S3)-(S5), $DOS(\omega)$ is the normalized phonon density of states. These equations have been shown to be accurate in capturing the alloy and impurity scattering for a lot of systems[5-9]. g_{mass} represents the alloying mass disorder induced by the mass difference between Bi and Sb atoms, given by

$$g_{mass} = \frac{\alpha_{Bi}}{\alpha_{Bi} + \alpha_{Sb}}\left(1 - \frac{M_{Bi}}{\bar{M}_{BiSb}}\right)^2 + \frac{\alpha_{Sb}}{\alpha_{Bi} + \alpha_{Sb}}\left(1 - \frac{M_{Sb}}{\bar{M}_{BiSb}}\right)^2, \quad \text{(S8)}$$

$$\bar{M}_{BiSb} = \frac{\alpha_{Bi}M_{Bi} + \alpha_{Sb}M_{Sb}}{\alpha_{Bi} + \alpha_{Sb}}, \quad \text{(S9)}$$

g_{Pb} represents the mass disorder induced by Pb, given by

$$g_{Pb} = \frac{\alpha_{Pb}}{\alpha_{Pb} + \alpha_{Bi} + \alpha_{Sb}}\left(1 - \frac{M_{Pb}}{\bar{M}}\right)^2, \quad \text{(S10)}$$

$$\bar{M} = \frac{\alpha_{Pb}M_{Pb} + \alpha_{Bi}M_{Bi} + \alpha_{Sb}M_{Sb}}{\alpha_{Pb} + \alpha_{Bi} + \alpha_{Sb}}, \quad \text{(S11)}$$

g_{other} represent the perturbation induced by the other defects in the samples, such as the bond change that was not included in the mass disorder, the antisite defects, dislocations, bond distortions, vacancies, etc. It is found that the $g_{other} = 0.43 g_{mass}$ give the best fitting.

The grain boundary scattering[6] in Eq. (S6) is determined by the grain diameter D multiplied by the specularity factor $F \in [1, \infty)$, which is related to the specularity parameter $p \in [0,1)$ by $F = \frac{1+P}{1-P}$. $F = 1$ or $p = 0$ represent the fully diffuse grain boundary, and $F = \infty$ or $p = 1$ represents the mirror-like grain boundary. For the three samples, the values of DF are fitted as

390 nm, 182 nm and 200 nm, respectively, which are similar to the 300 nm obtained in Ref. 11. By comparing DF with the grain diameter D estimated from X-ray diffraction experiment, we found that the specularity factor F is about 6. Writing in specularity parameter $p = \frac{F-1}{F+1}$, we got $p = 0.7$.

Finally, the lattice thermal conductivity can be calculated by the Boltzmann transport equation[6],

$$\kappa_l = \frac{4\pi}{3}\frac{1}{(2\pi)^3}\sum_{\nu}\left[\frac{2}{3}\int_x + \frac{1}{3}\int_z\right]\frac{\hbar^2\omega^2(\mathbf{k},\nu)}{k_B T^2}\frac{e^{\frac{\hbar\omega(\mathbf{k},\nu)}{k_B T}}}{(e^{\frac{\hbar\omega(\mathbf{k},\nu)}{k_B T}}-1)^2}v^2(\mathbf{k},\nu)\tau(\mathbf{k},\nu)k^2 dk \quad . \qquad \text{(S12)}$$

Note that in our model, only g_{mass} and DF are the fitting parameters, and all the others are predetermined. Since Bi_2Te_3 and Sb_2Te_3 are anisotropic, we choose the 2 times of crystalline-in-plane and 1 time of crystalline-cross-plane thermal conductivities to average. Note that the nano grain orientations in the nanocomposites are randomly distributed. The anisotropy between the in-plane and cross-plane thermal conductivity of the samples is induced by the different grain sizes in the two directions. In Eq. (S12), the summation of ν is typically taken over all the phonon branches. In Debye model, only the 3 acoustic phonon branches with linear dispersion relations will be considered, and thus it only works for the materials with zero or a few optical branches. The Bi_2Te_3 and Sb_2Te_3, however, have 3 dispersive acoustic branches and 12 optical branches, and it has been shown that the 4 low-energy optical phonon modes have a large contribution (50%) to the total lattice thermal conductivity. Thus, Debye model is not suitable for Bi_2Te_3 and Sb_2Te_3 anymore. In our work, we include all the 3 acoustic branches and the 4 low-energy optical branches.

To obtain the lattice thermal conductivity by Eq.(S12), the only data we need are the phonon dispersion and density of states, which can be obtained by first principles calculations using density functional theory (DFT)[10].

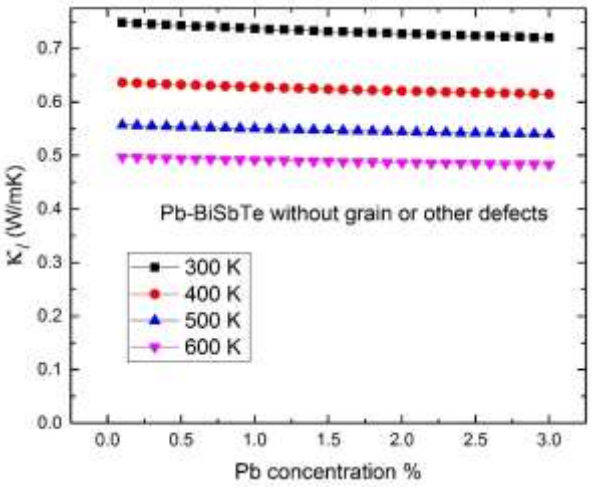

Figure S19. The lattice thermal conductivity of Pb-BiSbTe without grain or defects as a function of Pb concentration. This figure demonstrates the negligible influence of Pb impurity alone to the lattice thermal conductivity.

Table S2. The relative contribution from κ_l, κ_e, and κ_{bi} for the three samples at low and high temperatures.

	Low T (313 K)			High T (538 K for 1, 638 K for 2 & 3)		
	κ_l%	κ_e%	κ_{eh}%	κ_l%	κ_e%	κ_{bi}%
0.5%Pb	70	30	0	50	29	21
1.0%Pb	60	40	0	50	35	15
1.5%Pb	60	40	0	50	42	8

Estimate the hole mean free path

In degenerate semiconductor, the major carrier hole mean free path[12] is

$$\Lambda_h = \bar{\upsilon}_{th}\tau_h = \sqrt{\frac{3k_BT}{m^*}}\frac{m^*\mu}{e} = \sqrt{\frac{3k_BTm^*\mu^2}{e^2}}, \quad \text{(S13)}$$

and the hole mean free path is estimated at around 3 nm at room temperature.

Carrier transport modeling

We performed the Boltzmann transport equation (BTE) simulations with relaxation time approximation for the carrier transport analysis.[13] First, we fitted the density of states (DOS) obtained from first-principle band structure calculations based on density functional theory[14] with the modified Kane model:

$$E(1+\alpha E)=\frac{\hbar^2 k^2}{2m^*}, \qquad \text{(S14)}$$

where m^* is the effective mass, and α is the nonparabolicity. Two conduction bands and two valence bands were used to fit the DOS for Bi_2Te_3 over a wide energy range. The band structure parameters obtained are summarized in Table S3. More information about the DOS fitting is found elsewhere.[13]

Table S3. Band structure parameters used in our electronic BTE simulations. Data from literature[15] is also shown for comparison.

		Our parameters	Goldsmid (1950s)*
1st conduction band	m^*_{e1} (m_0)	0.66	0.58
	α_1 (eV^{-1})	0	0
2nd conduction band	m^*_{e2} (m_0)	0.69	–
	α_2 (eV^{-1})	1.0	–
Band offset between the two cond. bands	(eV)	0.23	–

1st valence Band	m^*_{h1} (m_0)	1.19	1.07
	α_3 (eV^{-1})	0.6	0
2nd valence Band	m^*_{h2} (m_0)	1.19	–
	α_4 (eV^{-1})	2.0	–
Band offset between the two val. bands	(eV)	0.27	–

All of the carrier transport properties are expressed as integral functions of the differential conductivity $\sigma_d(E)$ over carrier energy E, defined as

$$\sigma_d(E) = e^2\tau(E)v^2(E)\rho_{DOS}(E)\left(-\frac{\partial f_0}{\partial E}\right), \quad \text{(S15)}$$

where e is the electron charge, τ is the relaxation time, ρ_{DOS} is the density of states, v is the carrier velocity and f_0 is the Fermi-Dirac distribution. For the multiple-band transports in BiSbTe, the transport properties are calculated in each of the bands with the relative position of the Fermi level E_F from the band extremum and the contributions from each band are then added together to find the total transport values in the bulk. The electrical conductivity σ, the Seebeck coefficient S, and the electronic thermal conductivity are given, respectively, by

$$\sigma = \sum_i \int \sigma_{d,i}(E)dE, \quad \text{(S16)}$$

$$S = \sum_i \frac{1}{qT}\frac{\int \sigma_{d,i}(E)(E - E_{F,i})dE}{\sigma}, \quad \text{(S17)}$$

$$\kappa_{\text{elect}} = \sum_i \frac{1}{q^2T}\int (E - E_{F,i})^2 \sigma_{d,i}(E)dE - S^2\sigma T, \quad \text{(S18)}$$

where Σ is the sum over the bands, q is $-e$ for the conduction bands and $+e$ for the valence bands, T is the absolute temperature, and E_F is the Fermi energy. Carrier mobility of each type

is found from $\mu_h = \sigma_h/pe$ for holes, where p is the hole concentration, and $\mu_e = \sigma_e/ne$ for electrons, where n is the electron concentration. The Lorenz number is given by

$$L = \sum_i \frac{1}{q^2 T^2} \frac{\int \sigma_{d,i}(E)(E - E_{F,i})^2 dE}{\sigma} - S^2 . \quad \text{(S19)}$$

This Lorenz number is a function of band structure and the Fermi level (or carrier concentration). It is found that the Lorenz numbers for our Pb-doped BiSbTe samples are much lower (~1.6×10^{-8} W Ω K^{-2} for 1.0 % Pb at room temperature) than the conventional value for metals (~2.44×10^{-8} W Ω K^{-2}) due to the semiconducting behavior.

Subsequently, the total electrical conductivity and the total Seebeck coefficient in the two-type carrier transport are obtained by

$$\sigma = \sigma_e + \sigma_h , \quad \text{(S20)}$$

$$S = \frac{\sigma_e S_e + \sigma_h S_h}{\sigma_e + \sigma_h} , \quad \text{(S21)}$$

where the subscripts *e* and *h* denote the partial properties of electrons and holes, respectively. Since the partial Seebeck coefficients of electrons and holes possess the opposite signs, the magnitude of total Seebeck coefficient S is reduced by the bipolar transport. The total electronic thermal conductivity is not only the sum of the partial electronic thermal conductivities of electrons and holes. Another term from the bipolar thermodiffusion effect must be added to the total electronic thermal conductivity. The bipolar electronic thermal conductivity is given by

$$\kappa_{bi} = \frac{\sigma_e \sigma_h}{\sigma_e + \sigma_h}(S_e - S_h)^2 T . \quad \text{(S22)}$$

More detailed information about the carrier transport calculations for BiSbTe alloys is found in our recent paper, Ref. S13. In order to account for the effect of PbTe alloying in our composite material, we have adjusted the band gap of the nanocomposites with the

experimentally measured values in the BTE simulations, while the effective masses are fixed. In addition, the relevant carrier scattering parameters from the acoustic phonon deformation scattering, short-range defect scattering, and ionized impurity scattering have been further adjusted to fit the electrical conductivity of the samples. No additional parameters have been adjusted for Seebeck coefficient fitting.

References in supporting information

1. Slack, G. & Galginaitis, S. Thermal conductivity and phonon scattering by magnetic impurities in CdTe. *Phys. Rev.* **113,** 253 (1964).

2. Bessas, D. *et al.* Lattice dynamics in Bi2Te3 and Sb2Te 3: Te and Sb density of phonon states. *Phys. Rev. B - Condens. Matter Mater. Phys.* **86,** 224301 (2012).

3. Spitzer, D. P. Lattice thermal conductivity of semiconductors: A chemical bond approach. *J. Phys. Chem. Solids* **31,** 19–40 (1970).

4. Tamura, S. Isotope scattering of dispersive phonons in Ge. *Phys. Rev. B* **27,** 858 (1983).

5. Garg, J., Bonini, N., Kozinsky, B. & Marzari, N. Role of Disorder and Anharmonicity in the Thermal Conductivity of Silicon-Germanium Alloys: A First-Principles Study. *Phys. Rev. Lett.* **106,** 045901 (2011).

6. Feng, T. & Ruan, X. Prediction of Spectral Phonon Mean Free Path and Thermal Conductivity with Applications to Thermoelectrics and Thermal Management: A Review. *J. Nanomater.* **2014,** 206370 (2014).

7. Kamitakahara, W. A. & Brockhouse, B. N. Vibrations of a mixed crystal: Neutron scattering from Ni55Pd45. *Phys. Rev. B* **10,** 1200–1212 (1974).

8. Lindsay, L., Broido, D. a. & Reinecke, T. L. Thermal Conductivity and Large Isotope Effect in GaN from First Principles. *Phys. Rev. Lett.* **109,** 095901 (2012).

9. Feng, T., Qiu, B. & Ruan, X. Coupling between phonon-phonon and phonon-impurity scattering: A critical revisit of the spectral Matthiessen's rule. *Phys. Rev. B* **92,** 235206 (2015).

10. Chis, V. *et al.* Vibrations in binary and ternary topological insulators: First-principles calculations and Raman spectroscopy measurements. *Phys. Rev. B* **86,** 174304 (2012).

11. Kim, S. I. *et al.* Dense dislocation arrays embedded in grain boundaries for high-performance bulk thermoelectrics. *Science (80).* **348,** 109–114 (2015).

12. Zheng, J. *et al.* Synthesis and high temperature thermoelectric properties of Yb0.25Co4Sb12-(Ag2Te)x(Sb2Te3)1−x nanocomposites. *Front. Chem.* **3,** 53 (2015).

13. Bahk, J.-H. & Shakouri, A. Minority carrier blocking to enhance the thermoelectric figure of merit in narrow band gap semiconductors. *Phys. Rev. B* **93**, 165209 (2016).

14. Jeong C, Kim R, Luisier M, Datta S, Lundstrom M. On Landauer versus Boltzmann and full band versus effective mass evaluation of thermoelectric transport coefficients, *J. Appl. Phys.* **107,** 023707 (2010).

15. S. NG, J. S, J. GH. Thermoelectrics: Basic Principles and New Materials Developments. Springer-Verlag: Berlin, 2001.